**RESEARCH ARTICLE**

# Effect of 3D-bioprinted droplet impact dynamics on a pre-printed soft hydrogel matrix

Xinxing Chen[1] · Aidan P. O'Mahony[2] · Tracie J. Barber[1]

## Abstract

3D droplet-based bioprinting technology is an innovative and time-saving method to precisely generate cell laden 3D structures for multiple clinical and research applications. It is important that the printed droplet must impact so as to leave a single isolated drop, for high printing resolution and accuracy. Therefore, understanding the criteria that control spreading behaviour and prevent droplet splashing is of great importance in optimizing the printing performance. In this experimental work, the physics of the impact of bioink droplets on a pre-printed soft hydrogel matrix was investigated. The droplet size, velocity, and input cell density were varied to generate a range of droplet impact behaviours. It has been shown that the soft substrate inhibited the droplet spreading after impact. The deposition/splashing boundary on the dry/wet flat surface (Nunclon $^{TM}$ Delta surface-treated plastic) was defined by $K = \text{We}^{0.5}\text{Re}^{0.25} = 86.19$. The splashing threshold on the soft hydrogel matrix was defined by $K = 44.78$ and $L = \text{WeRe}^{-0.4} = 13.85$ for both blank and cell-laden inks on dry/wet soft substrates. Beyond this threshold, the printed droplet volume will be much lower than the expected volume due to splashing, leading to poor printing performance. The absolute splashing threshold on the dry/wet soft hydrogel matrix was defined by $K = 73.41$ and $L = 27.36$. The printed 3D cell-laden structures were also presented to illustrate how the impact behaviours influence the possible printing fidelity and structure integrity.

## 1 Introduction

Three-dimensional (3D) bioprinting is an innovative technology for the fabrication of artificial tissues and organs. Functional biological 3D structures are formed by depositing biological materials, biochemicals and living cells, layer-by-layer, from the bottom up (Murphy , Atala 2014; Derakhshanfar et al. 2018; Chameettachal et al. 2019; Mobaraki et al. 2020; Vanaei et al. 2021).

Aidan P.O'Mahony and Tracie J.Barbe have contributed equally.

✉ Xinxing Chen
 xinxing.chen@student.unsw.edu.au

 Aidan P. O'Mahony
 aidan@inventia.life

 Tracie J. Barber
 t.barber@unsw.edu.au

1 School of Mechanical and Manufacturing Engineering, University of New South Wales, Kensington, Sydney, NSW 2052, Australia

2 Inventia Life Science Pty Ltd, Alexandria, Sydney, NSW 2015, Australia

The need for bioprinting is supported by the several emerging application fields, including tissue engineering (Gudapati et al. 2016; Saygili et al. 2020; Machekposhti et al. 2020; Li et al. 2020; Vanaei et al. 2021; Bejoy et al. 2021), regenerative medicine (Gudapati et al. 2016; Saygili et al. 2020; Vanaei et al. 2021; Bejoy et al. 2021), high-throughput screening (Gudapati et al. 2016; Saygili et al. 2020; Machekposhti et al. 2020; Li et al. 2020; Bejoy et al. 2021), pharmaceutics and drug testing (Gudapati et al. 2016; Chameettachal et al. 2019; Machekposhti et al. 2020; Vanaei et al. 2021; Bejoy et al. 2021), and physiological/pathological modeling (Ouyang et al. 2016; Vanaei et al. 2021). The four main 3D bioprinting approaches are droplet-based bioprinting (inkjet, acoustic, microvalve, and electrohydrodynamic bioprinting) (Gudapati et al. 2016, Ng et al. 2017; Xu et al. 2019; Saygili et al. 2020; Ng et al. 2020; Mobaraki et al. 2020; Zhang et al. 2021; Vanaei et al. 2021; Bejoy et al. 2021), extrusion-based bioprinting (Gudapati et al. 2016; Saygili et al. 2020; Mobaraki et al. 2020; Zhang et al. 2021; Vanaei et al. 2021; Bejoy et al. 2021), laser-based bioprinting (Gudapati et al. 2016; Xu et al. 2019; Saygili et al. 2020; Mobaraki et al. 2020; Zhang et al. 2021; Vanaei et al. 2021; Bejoy et al.

2021), and vat polymerization (stereolithography, digital light processing and two-photon polymerization) (Ng et al. 2020; Vanaei et al. 2021; Yilmaz et al. 2021; Bejoy et al. 2021). The need for precise (Gudapati et al. 2016; Saygili et al. 2020; Bejoy et al. 2021), flexible (Gudapati et al. 2016; Saygili et al. 2020; Yilmaz et al. 2021), low-cost (Gudapati et al. 2016; Chameettachal et al. 2019; Mobaraki et al. 2020; Saygili et al. 2020; Bejoy et al. 2021), compatible (Gudapati et al. 2016; Mobaraki et al. 2020; Saygili et al. 2020), reliable (Ng et al. 2017; Chameettachal et al. 2019; Mobaraki et al. 2020), and high-throughput production of cell-laden structures (Ng et al. 2017; Chameettachal et al. 2019; Mobaraki et al. 2020; Saygili et al. 2020; Bejoy et al. 2021) bolsters droplet-based bioprinting's growing importance in the field.

The essential idea for droplet-based 3D bioprinting is to print bioink droplets with precise control to create 3D structures on the substrate (Murphy , Atala 2014; Liu and Derby 2019; Mobaraki et al. 2020; Vanaei et al. 2021). The first step in the process is to manufacture bioink with defined fluid properties for successful droplet printability. The biomaterials must be printed onto a substrate or a previously printed solidified layer and undergo a phase transition: becoming a solid deposit and forming the desired structural features. To produce 3D structures, the deposition and solidification processes must be repeated (Derby 2010; Gong et al. 2020).

Ultimately, droplet-based bioprinting requires the precise control of the printed pattern and shape. Thus, understanding the impingement of a droplet onto a solid surface, or previously deposited material, is crucial as it provide insights regrading printing resolution and structural integrity (Gudapati et al. 2016; Gong et al. 2020). The two major impingement characteristics are the spreading and splashing of the droplet. For the former, the droplet spreads over the impact surface due to its kinetic energy and surface energy interactions between the droplet and the substrate. This consequently affects the bioprinting resolution. For high initial droplet kinetic energy, the droplet is not fully captured by the impact substrate; the droplet breaks into secondary droplets after collision, which is caused splashing (Yarin 2006; Derby 2010; Gudapati et al. 2016; Ng et al. 2017). Splashing of the droplet results in displacement of the deposited biomaterial from the ideal position and may also cause structural failure or cross-contamination in 3D bioprinting (Derby 2010; Gudapati et al. 2016).

The dynamics of liquid droplet impingement onto a surface, is mainly influenced by the bioink and substrate properties, and impact velocity (Mao et al. 1997; Yarin 2006; Gudapati et al. 2016; Ng et al. 2017). The maximum droplet spread and critical conditions for splashing are characterized by two non-dimensional parameters. The Reynolds number, *Re*, and the Weber number, *We*, defined as:

$$\text{Re} = \frac{\rho v D}{\mu} \tag{1}$$

$$\text{We} = \frac{\rho v^2 D}{\gamma} \tag{2}$$

where $\rho$, $v$, $\mu$, and $\gamma$ are the fluid density, impact velocity, dynamic viscosity, and surface tension, respectively; $D$ is the characteristic length, here taken as the initial droplet diameter $D_o$.

Mao et al. found that the maximum spread of a droplet upon impact depends strongly on the liquid viscosity and the impact velocity on solid substrates. The maximum spread increases with an increase in the Reynolds number and the Weber number (Mao et al. 1997). Derby (Derby 2010) has summarized that the threshold for the onset of splashing on flat, smooth surfaces is $K = \text{We}^{0.5}\text{Re}^{0.25} > 50$. On wet, flat surfaces, Weiss and Yarin (Weiss and Yarin 1999) have found that the threshold of splashing with a crown shape is $We \gg 40$. Most of the previous works consider a relatively small Weber number to reduce or eliminate the splashing on dry/wet flat surfaces(Weiss and Yarin 1999; Yarin 2006; Howland et al. 2016; Gudapati et al. 2016; Li et al. 2020). Ng et al. (Ng et al. 2022) printed cell-laden droplets directly onto a pre-printed thin liquid film using an inkjet-based 3D bioprinter and found a splashing threshold of $\text{We}^{0.5}\text{Re}^{0.17} = 63$. Moreover, the increase in input cell density helps to mitigate droplet splashing and improve the printing fidelity (Ng et al. 2022).

In 3D bioprinting, the previously printed layer can be viewed as a soft elastic substrate. The dynamics of droplets impinging on soft substrates is different from the case of flat surfaces. Howland et al.(Howland et al. 2016) found that the additional energy dissipation due to surface deformation during droplet impact on soft surfaces can reduce or even suppress splashing with Weber number lower than 300. Basso and Bostwick (Basso and Bostwick 2020) studied water and ethanol drops impacting on soft elastic substrates with a large range of elasticities. They found that soft substrates inhibit droplet spreading after impact. The splashing threshold as defined by $K = \text{We}^{0.5}\text{Re}^{0.25}$, increases as the substrate elasticity decreases, indicating that it is harder to splash on soft substrates. For soft substrate with elasticity lower than 1 kPa, the splashing threshold is lower than 175. Kittel et al. (Kittel et al. 2018) described the deposition/splashing threshold on thin soft elastic surfaces as $L = \text{We}\text{Re}^{-0.4} = 16.8$. They also found that the threshold does not depend on the rheological properties of the deformable layer, by studying the impact phenomena of glycerin-water droplets on different thin viscoelastic surfaces.

Although an extensive effort has been devoted to understanding drop impingement on flat and thin soft surfaces

(the dimensionless substrate thickness $\delta = h_o/D_o < 1$) (Kittel et al. 2018), 3D-bioprinted droplet impact behaviour on pre-printed thick soft structures ($\delta = h_o/D_o > 1$) and the corresponding coupling mechanics of liquid-gel interaction still require further study. To fully understand the processes of 3D-bioprinted droplet deposition and fusion, hydrogel droplets were printed and chemically cross-linked using a commercial micro-valve-based 3D bioprinting platform (RASTRUM™), provided by Inventia Life Science Pty Ltd.[1] Hydrogels have been used extensively in droplet-based 3D bioprinting due to good printability, good cell compatibility, and capacity to mimic the extracellular matrix (ECM) environment for cellular activities (Gudapati et al. 2016; Hospodiuk et al. 2017; Chameettachal et al. 2019; Unagolla and Jayasuriya 2020; Li et al. 2020). Hydrogel droplets should solidify immediately after landing to help mechanically support the subsequent layer (Hospodiuk et al. 2017; Catros et al. 2011). Solidification occurs by cross-linking of polymer chains in an aqueous medium through various mechanisms such as physical entanglement, ionic interaction, and chemical cross-linking (Unagolla and Jayasuriya 2020).

The bioprinting platform was previously reported for the high-throughput production of 3D cell spheroids, providing more *invivo* realistic models (Utama et al. 2021). Sodium alginate bioink and calcium chloride (CaCl₂) activator were firstly printed as a tissue-like matrix, which has the structural stability to support gravity-based cell spheroid formation. The tissue-like matrix also supports control over cell spheroid number, size, and shape so that statistically reliable data on drug responses can be obtained in the future (Utama et al. 2020). Four-arm poly(ethylene glycol) maleimide (PEG-4MAL) hydrogels and cell-containing bis-thiol-PEG cross-linker were alternately printed on the top of hydrogel matrix. The combination of matrix support, gravitational forces, and ECM secreted by cells-assisted cell migration, adhesion and proliferation during incubation, leading to cell spheroid formation (Utama et al. 2020, 2021). In this paper, the drop impingement on a pre-printed hydrogel matrix was studied. The effect of different bioprinter operating conditions, substrates, and input cell density on droplet impact dynamics were experimentally evaluated using a high-speed imaging system. The droplet impact on the pre-printed soft hydrogel matrix reflects the real impact process in 3D droplet-based bioprinting, considering the surface condition, thickness, and stiffness of the matrix generated from actual prints. The formed 3D cell spheroids were also presented under different conditions, potential improvements in printing fidelity and structural integrity are also discussed.

## 2 Materials and methods

### 2.1 Ink preparation

Four commercially available ink solutions were used to produce the 3D cell spheroid assay and evaluate the droplet impact dynamics. The alginate bioink was formulated from sodium alginate in Milli-Q water and Dulbecco's buffered saline (DPBS). The hydrogel matrix can be fabricated by printing calcium chloride (CaCl₂) activator, a mixture of calcium chloride and Milli-Q water, onto the alginate solutions. The four-arm PEG-based bioink, as a linear polyether compound, was produced by mixing ethylene glycol with Milli-Q water. The corresponding bis-thiol activator, used as the cell-carrier ink during the 3D bioprinting process, contains short chain bis-thiol peptide cross-linker dissolved in DPBS. The actual sequence, concentration and formation process of the inks are proprietary to Inventia Life Science Pty Ltd. The ink solutions were stored at $-20\,°C$. All solutions were sterilised by filtration through a $0.22\,\mu m$ syringe filter prior to use.

To study the effect of cells on droplet impact, the cell-laden ink used in this study was obtained by suspending $1 \times 10^7$ cells/ml cell concentration in the blank bis-thiol activator. MCF-7 breast cancer cells were cultured in Dulbecco's minimum essential media (DMEM, Gibco®, Australia) supplemented with 10% fetal bovine serum (FBS, Gibco®, Australia) and 2% antibiotic-antimycotic (Gibco®, Australia) at $37\,°C$ and 5% $CO_2$. Cells were screened and passaged every three days. The living cells were harvested from the flasks with initial cell counts achieved using a hemocytometer and the cell pallets with desired cell number were obtained after centrifuging. The blank ink (thiol-containing activator) was mixed with the cell pellets to make the final cell-laden bioinks with a cell density of $1 \times 10^7$ cells/ml. The cell concentration was checked using a hemocytometer before tests.

The mean fluid density was obtained following a method published by Liu, et al. (Liu and Derby 2019) 1 ml aliquots of the inks were extracted using a 1 ml adjustable-volume pipette and weighed by a laboratory balance. The liquid density was calculated from the measured volumes and weights. The mean liquid viscosity was measured using a vibro viscometer (SV-10A, A &D, Japan) at 25 °C. The pendant drop surface tension measurement technique (Arashiro and Demarquette 1999; Berry et al. 2015) was implemented in this study to measure the surface tension of the inks using a drop shape analyser (DSA30E, *KRÜSS*) at 25 °C.

---

[1] https://inventia.life/

**(i)**



**(ii)**
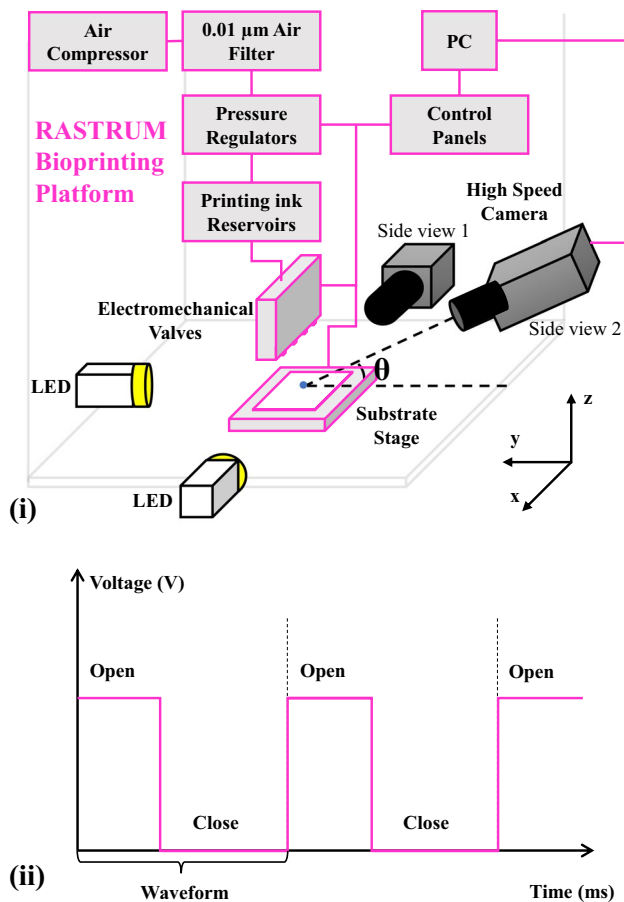
**Fig. 1 i** Schematic diagram of experimental set-up; **ii** Schematic of the waveform used with the microvalve-based bioprinting system

## 2.2 Bioprinting platform

The micro-valve-based 3D bioprinting platform incorporated a substrate stage, a fly-by printhead composed of multiple electromechanical valve dispensers, ink reservoirs, control panels, pressure regulators, a 0.01 $\mu$m air filter, and a pneumatic back pressure supplier can be seen in Fig. 1i. To eject ink droplets, a constant pneumatic pressure was applied inside of the printing valve, and a step voltage pulse (Fig. 1ii) was applied to activated the electromechanical valve, generating a magnetic field that pulled the plunger upwards from the guarded orifice. Thus, the pressure is applied to the valve only when the valve is activated. This pressure overcomes the forces due ink viscosity and surface tension causing the ink solution to be ejected through the orifice (Gudapati et al. 2016; Ng et al. 2017).

Dosing energy (*La*) is defined as the integral of the applied pneumatic pressure *P*(*t*) over valve opening time *dt* (Eq.(3)). This parameter has a positive correlation with the resulting droplet volume and velocity (Klinger et al.

2020; Chen et al. 2021; 2022), and can be used to describe the bioprinter's operating condition.

$$E_d = \int P(t)dt \tag{3}$$

The basic unit for dosing energy is Laske (*La*).

$$[E_d] = 1La = 0.1kPa \times 1ms \tag{4}$$

All ink solutions were brought to room temperature prior to printing. The micro-valve-based 3D bioprinting platform was sterilised and rinsed with 70% Ethanol solution (left in the system for at least 20 min) and filtered deionized (DI) water. After sterilization, the sodium alginate bioink (Ink A), CaCl$_2$ activator (Ink B), PEG-4MAL bioink (Ink C), and bis-thiol activator (Ink D) were pipetted into respective reservoirs. To study the influence of cells on droplet impact, the bis-thiol activator was divided into a blank ink sample and a cell-laden sample with $1 \times 10^7$ cells/ml input cell concentration.

The bioprinting platform utilized a fly-by printing method using proprietary custom-made software. The dosing energies applied on the four valves were set separately. During fly-by printing, the printhead travelled on the x-axis at a constant velocity. The hydrogel matrix layer was printed first, by initially ejecting a row of sodium alginate bioink (Ink A) drops in one well of the Nunclon ™ Delta surface 96-well plate (Sigma-Aldrich, Australia) as the printhead travels on the positive x-axis direction (Fig. 2i). The well plate was placed approximately 20 mm away from the valve orifice. On the return flight, CaCl$_2$ activator (Ink B) droplets were printed on top of the bioink droplets to initiate the hydrogel formation (Fig. 2ii). Upon contact, gelation occurred instantaneously forming 3D structures (Fig. 2iii). The process was repeated at different y locations until the target well was covered by a continuous hydrogel layer (Fig. 2iv).

A drop of PEG-4MAL bioink (Ink C) was printed at the desired location (Fig. 2v) which was quickly followed by printing a drop of blank or cell-laden bis-thiol activator (Ink D) at the same location to initiate the cross-linking process (Fig. 2vi and vii). Variation of the size of the 3D-bioprinted hydrogel bead was achieved by altering the dosing energy. The formed 3D hydrogel structures match the mechanical and biochemical properties of different types of tissue, which can provide a physiologically relevant matrix environment for cultured cells (Utama et al. 2021; Engel et al. 2022).

A dry, flat surface was used as a contrast substrate in this study. Ink C and Ink D were printed directly into the Nunclon ™ Delta surface 96-well plate, which can be seen as a plastic surface undergoes Nunclon ™ Delta surface treatment, without printing the gel substrate first.
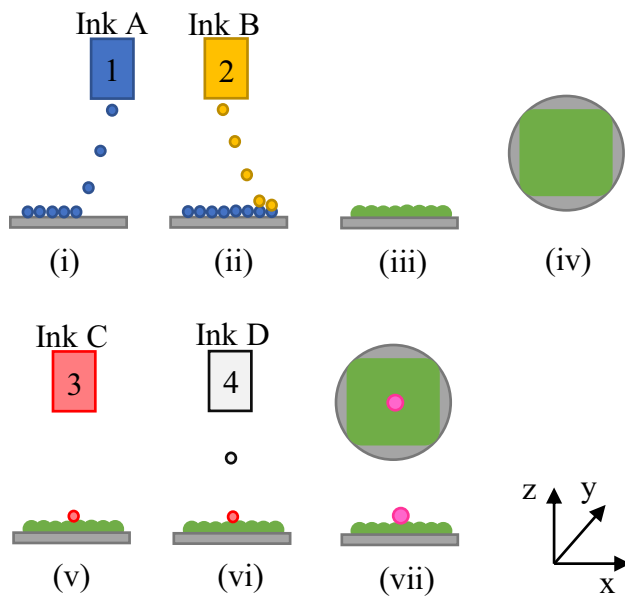
**Fig. 2** Illustration of the fly-by bioprinting process: **i** The printing valve 1 loaded with sodium alginate bioink (Ink A) ejects a row of bioink droplets while travelling on the positive x-axis direction;**ii** The printing valve 2 loaded with $CaCl_2$ activator (Ink B) ejects a row of activator droplets on top of the bioink drops while travelling on the negative x-axis direction; (iii) Gelation occurs and forms into a row of hydrogel; (iv) Formation of a layer of hydrogel matrix; (v) The printing valve 3 loaded with PEG-4MAL bioink (Ink C) ejects a single bioink droplet on top of the hydrogel matrix while travelling on the positive x-axis direction; (vi) The printing valve 4 loaded with blank or cell-laden bis-thiol activator (Ink D) ejects a single bioink droplet on top of the bioink drop while travelling on the negative x-axis direction; (vii) Gelation occurs and forms into a blank or cell-laden hydrogel bead

In this study, Ink A (sodium alginate bioink) and Ink B ($CaCl_2$ activator) were printed under constant dosing energies, aiming to achieve the same hydrogel substrate structure. To investigate the influence of operating conditions on droplet impact, eight sets of the bioprinter operating conditions were tested on Ink C (PEG-4MAL bioink), blank Ink D (bis-thiol activator), and cell-laden Ink D (bis-thiol activator), with dosing energy ranging from 1.51 to 3.36 La.

At the completion of the printing process with cell-laden Ink D, 200 $\mu$l DMEM supplemented with 10% FBS and 2% antibiotic-antimycotic was added manually in the well. The plate was then ready for incubation at 37 °C and 5% $CO_2$ and visualization of the printed 3D cell structures.

## 2.3 High-speed imaging system

The printing platform was imaged with a high-speed camera system, including a high-speed camera FASTCAM SA-X2 (Photron[TM]), a macro lens (55 mm f/2.8, Nikon[TM]), and 68 mm extension tubes (Kenko[TM]) (Fig. 1i). And a LED illuminator is used for shadowgraphy droplets in-flight and the droplet impingement processes. The high-speed imaging system visualized the droplet impact dynamics in two directions separately: (1) Side view 1, where the camera was pointing at positive x-axis direction and the LED illuminator was pointing at negative x-axis direction and directly facing towards the lens; (2) Side view 2, where the camera was aimed $\theta = 20°$ below the horizontal at positive y-axis direction to obtain clear images of the droplet spread upon impact. The LED illuminator in Side view 2 was facing towards the negative y-axis. Shadowgraph droplet images were recorded at 50,000 frames per second (fps) frame rate with $256 \times 128$ pixels image resolution. The resulting image height to pixel ratio (HTPR) was 15.5 $\mu$m/pixel.

The impact of a droplet on a substrate consists four stages: initial, spreading, contracting and equilibrium (Mallinson et al. 2018) (Fig. 3). Droplet size and falling velocities in the initial stage before impact were analysed from the captured shadowgraph images using a custom image processing program in MATLAB®2018b as previously reported. The image processing program produces a clear droplet edge detection among the diffraction region in the shadowgraph images. The theory of droplet edge detection has been detailed in the previous study (Chen et al. 2021) and is not described here. After applying the edge detection method, the droplet was separated from the background with a clean edge. At the droplet image captured location (20 mm away from the orifice), the droplets coalesce into near spheres due to the effect of surface tension (Klinger et al. 2020) and function *imfindcircles* detects circular
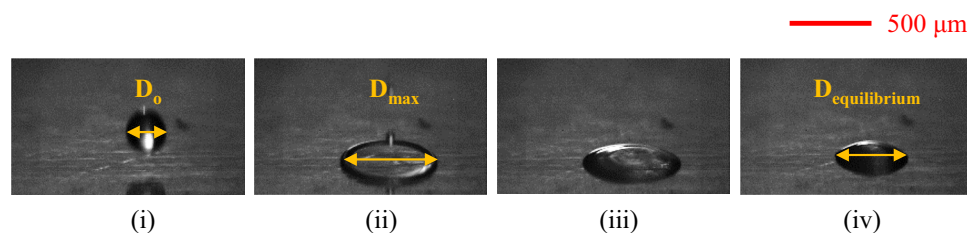


**Fig. 3** Four impact stages: **i** Initial stage, droplet with a diameter of $D_o$; **ii** Drop spreading to a maximum diameter $D_{max}$; **iii** Contracting stage; **iv**Equilibrium stage, where drop retracts to an equilibrium diameter $D_{equilibrium}$. Scale bar: 500 $\mu$m
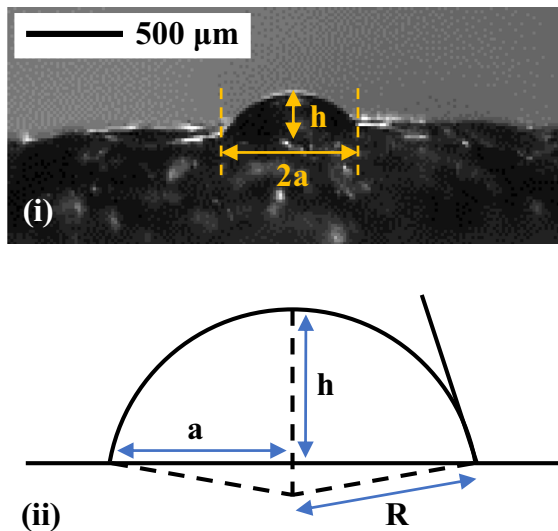
**Fig. 4** Illustration of the droplet size measurement: **i** Measurement of droplet equilibrium diameter and equilibrium height. Scale bar: 500 $\mu$m; **ii** Volume calculation of the equilibrium droplet, where $R$ is the radius of the spherical cap

objects in the image using a circular Hough transform (Kang et al. 2020). In this manner, the centre position and dimension $D_o$ of the droplet based on the assumption of sphericity were obtained directly using this function and the droplet falling velocity $v_o$ before impact was calculated using the change in droplet centroids positions between each pair of frame.

$$v_o = \frac{\Delta z}{\Delta t} \qquad (5)$$

where $\Delta z$ is the distance travelled in the vertical direction calculated from the positions of droplet centroids between consecutive images, $\Delta t$ is the interval time between consecutive frames.

The edge detection program could not be applied to the droplet impact images due to the low contrast between the hydrogel matrix and hydrogel droplet (as shown in Fig. 4i). Therefore, measurement of the droplet spreading diameter, equilibrium diameter, and equilibrium height was conducted manually using the open source program ImageJ with a $\pm$ 2 pixel error. The measurement error was used in the subsequent calculation for the deviation of equilibrium droplet volume (Eq. 6).

$$V_h = \frac{1}{6}\pi h(3a^2 + h^2) \qquad (6)$$

where the droplet equilibrium volume is assumed to be a spherical cap with height $h$, and radius $a$ of the base circle of the cap.

## 2.4 Printed 3D cell structure visualization

To investigate the influence of printing conditions on the printed cell-laden 3D structure, bright field images were immediately obtained using an inverted microscope. The next step was to demonstrate the long-term proliferation profile of the printed cells. The printed cell-laden structures were cultured over a period of 7 days inside an incubator. The Hoechst 33342 fluorimetric assay (ThermoFisher, Australia) was used to demonstrate the proliferation profile of printed cells based on staining all cell nuclei (DNA) using a blue fluorescence dye, enabling visualisation of all cells. DPBS was placed in wells before the addition of the Hoechst 33342 fluorimetric assay in the ratio of 2000: 1. A live/dead assay (Utama et al. 2021) was also performed using Calcein-AM (Biotium, USA) and Ethidium homodimer-III (Biotium, USA). Calcein-AM and Ethidium homodimer-III dilution with a ratio of 1: 2000 and 1: 1000 were added in the wells, followed by incubation at 37 °C for 30 min. Calcein-AM is internalised by viable cells and converted to calcein (a green flourescent compound) in the cell cytoplasm. Ethidium homodimer-III only enters dead cells and becomes a red fluorescent compound upon binding to DNA, therefore, the stained green cells represent viable cells, whereas the stained red cells represent dead cells. A fluorescent microscope was used to excite the Hoechst 33342 fluorimetric assay, Calcein-AM, and Ethidium homodimer-III at wavelength of 350, 488, and 594 nm, respectively, for the fluorescence imaging.

# 3 Results and discussion

## 3.1 Characterization of printing conditions

### 3.1.1 Droplet diameter and velocity before impact

To study the effects of dosing energy on droplet impact dynamics, high speed images of droplets just before impingement were captured and analysed to obtain the droplet diameter $D_o$ and falling velocity $v_o$. PEG-4MAL bioink (Ink C), was the first to impact on the soft elastic hydrogel matrix, and it was ejected under eight dosing energies: 1.68 La, 1.92 La, 2.16 La, 2.4 La, 2.64 La, 2.88 La, 3.12 La, and 3.36 La. To initiate the hydrogel formation, blank or cell-laden bis-thiolactivator (Ink D) was printed on top of the Ink C drops under eight matching dosing energies, respectively. It was found that to achieve the optimum gelation result, the PEG-4MAL bioink and the bis-thiol activator should be printed at 1:1 ratio (Utama et al. 2021). At this ratio, the formed hydrogel can mechanically support the 3D structure without collapsing. In droplet ejection, more energy is needed for ink with higher physical properties to overcome the ink viscosity and surface tension at the orifice to achieve
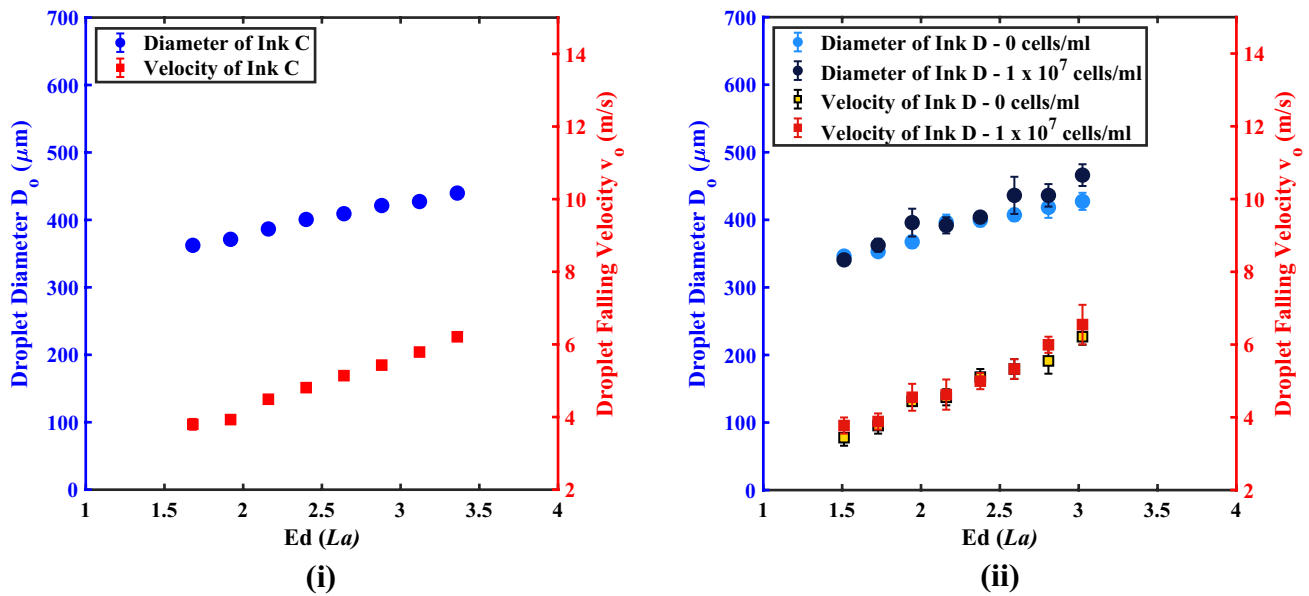
**Fig. 5** **i** The initial droplet diameter ($\mu$m) and falling velocity (m/s) before impact of bioink Ink C under dosing energy ranging from 1.68 to 3.36 La; **ii** The initial droplet diameter ($\mu$m) and falling velocity (m/s) before impact of activator Ink D with/without cells under dosing energy ranging from 1.51 to 3.02 La

the target size (Gudapati et al. 2016; Ng et al. 2017). Therefore, the printing energy for Ink D should be slightly lower than the ones applied on Ink C, which has higher physical properties than Ink D, to achieve the 1:1 ratio between the size of Ink C and Ink D. The dosing energies applied on Ink C ranged from 1.51 to 3.02 La.

The droplet diameter and falling velocity of printed Ink C, blank Ink D, and cell-laden ink D under eight sets of bioprinter operating conditions are depicted in Fig. 5. In all cases, the droplet diameter increased with increasing dosing energy. The initial droplet diameter $D_o$ of the ejected Ink C increased from $362.31 \pm 1.50 \mu$m under 1.68 La to $439.76 \pm 1.09 \mu$m under 3.36 La. Blank Ink D had the initial droplet diameter as $346.32 \pm 4.44 \mu$m under 1.51 La, which was similar to the size of printed bioink droplet for the optimum hydrogel formation outcome. Under 3.02 La, initial droplet diameter of the blank Ink D increased to $427.35 \pm 12.66 \mu$m. Seeded with a high input cell concentration ($1 \times 10^7$ cells/ml), the droplet diameter of Ink D increased from $340.77 \pm 4.44 \mu$m under 1.51 La, to $466.20 \pm 16.09 \mu$m under 3.02 La. The average size difference between 0 cells/ml and $1 \times 10^7$ cells/ml was $17.23 \pm 11.63 \mu$m under all dosing energies. There is no clear increasing or decreasing tendency with cell concentrations in droplet size. Input cell concentration up to 10 million cells/ml can be seen to have negligible impact on droplet size under the chosen dosing energies in micro-valve-based bioprinting. A similar result was reported by our previous study (Chen et al. 2022).

Droplet falling velocity also has a positive correlation with the applied energy, which is the dosing energy in the micro-valve-based bioprinting. By increasing the applied pneumatic pressure or valve opening time, the dosing energy increases accordingly (Eq. 3). High dosing energy leads to high droplet falling velocity. From 1.68 to 3.36 La, bioink C has a near linear increasing droplet falling velocity raising from $3.8 \pm 0.15$ to $6.21 \pm 0.08$ m/s accordingly. The velocities just before the blank Ink D droplet impact increased from $3.44 \pm 0.22$ to $6.22 \pm 0.22$ m/s under the corresponding matching dosing energies. Similar to the droplet size, the input cell concentration has negligible impact on the droplet velocity, leading to $3.77 \pm 0.22$ to $6.55 \pm 0.54$ m/s in the tested dosing energy range. Cell-laden droplets showed no significant larger or smaller velocity values than the droplets containing no cells. The average velocity difference between 0 cells/ml and $1 \times 10^7$ cells/ml was $0.3 \pm 0.18$ m/s under all dosing energies.

### 3.1.2 Ink physical properties and dimensionless numbers

The viscosity of the blank Ink C and Ink D were measured by Inventia Life Science Pty Ltd, under 75, 225, and 675 1/s shear rate with a constant value. Therefore, both blank Ink C and Ink D can be treated as Newtonian fluids. The viscosity of the cell-laden Ink D was measured at a fixed shear rate ($10^3$ 1/s). Ng and Huang (Ng et al. 2022) found that the increasing shear rate results in lower average viscosity for cell-laden inks. The reduction becomes less significant at higher shear rates ($> 10^3$ 1/s) (Ng et al. 2022). The printing

**Table 1** Average fluid physical properties of the blank activator Ink D and the cell-laden Ink D with $1 \times 10^7$ cells/ml cell concentration

| Ink | Density (kg m$^{-3}$) | Dynamic viscosity (mPa s) | Surface tension (mN/m) |
|---|---|---|---|
| Blank ink D[1] | – | – | – |
| Cell-laden ink D | ↑ 2.7% | ↑ 5.7% | ↓ 13.4% |

[1] Measured values are proprietary to the provider and not available

process provided an estimated $10^3$ 1/s shear rate on cell-laden Ink D during ejection under varying dosing energies. Therefore, the measured average viscosity for cell-laden Ink D is representative of the shear rate experienced by the cell-laden Ink D during the printing process.

The actual value of density, viscosity, and surface tension of Ink C, Ink D, and cell-laden Ink D are proprietary to the provider. The percentage changes between the blank activator Ink D and the cell-laden Ink D are listed in Table 1 instead.

The density value of the cell-laden Ink D increased by 2.7% compared to the blank Ink D. By adding cells to the ink, the resulting higher frictional force and distorted flow field at the ink-cell interface leads to an increase in the fluid viscosity (Ng et al. 2022). The viscosity of cell-laden Ink D increased 5.7% compared to the blank ink. Theoretically, the higher viscous dissipation during droplet formation process results in a lower overall droplet size and velocity (Xu et al. 2014; Ng et al. 2017, 2022). The increased percentage of the cell-laden ink viscosity was small (5.7%) compared to the blank ink, leading to negligible influence on the droplet size and falling velocity. In contrast, the average surface tension of cell-laden activator decreased 13.4% compared to the blank Ink D, due to the reduction in total free energy of the bioink, because more cells were absorbed to the interface (Xu et al. 2014; Ng et al. 2017). Xu, et al. (Xu et al. 2014)

and Ng, et al. (Ng et al. 2017, 2022) have also found that increasing cell concentration results in a decreased surface tension, and an increased density and viscosity.

Although the value of measured density, viscosity, and surface tension of Ink C, Ink D, and cell-laden Ink D cannot be presented in this paper, they were used to calculate the Weber number and Reynolds number to help quantify the study. Table 2 lists the Weber number, We, and the Reynolds number, Re, calculated from the measured droplet size, falling velocity, and physical properties (measured density, viscosity, and surface tension of Ink C, Ink D, and cell-laden Ink D) under eight sets of printing conditions.

Due to the difference in ink physical properties, the Weber number and the Reynolds number of cell-laden Ink D was higher than the blank Ink D under all printing conditions. The values of Re and We increased with increasing dosing energy value.

### 3.1.3 Substrate properties

Two substrates were used in this study: (1) Nunclon ™ Delta surface 96-well plate, which can be seen as a flat solid substrate; (2) pre-printed hydrogel matrix, which can be seen as a soft elastic substrate. To generate the hydrogel matrix, the sodium alginate bioink (Ink A), followed by the CaCl$_2$ activator (Ink B), was printed directly in the well plate. The thickness of the printed hydrogel matrix was $h_o = 648.73 \pm 33.07$ $\mu$m, measured from the obtained images. The obtained maximum initial droplet diameter $D_o$ was $466.20 \pm 16.09$ $\mu$m, leading to the dimensionless substrate thickness $\delta = h_o/D_o > 1.4$. The pre-printed hydrogel matrix can be seen as a thick ($\delta > 1$) soft elastic structure (Kittel et al. 2018), which mimics the 3D bioprinting conditions in practice. Based on the providers' research, the elastic modulus of the hydrogel matrix generated under this printing condition is slightly over 1.5 kPa (Mahmodi et al. 2021).

**Table 2** Weber number, We, and Reynolds number, Re, of the inks under eight sets of bioprinter operating conditions. The dosing energy values for Ink C and Ink D in each set are listed, respectively

| | Ink C[a] | | | | Ink D[b] seeded with 0 cells/ml | | Ink D seeded with $1 \times 10^7$ cells/ml | |
|---|---|---|---|---|---|---|---|---|
| Set | $E_d$ - Ink C (La) | We | Re | $E_d$ - Ink D (La) | We | Re | We | Re |
| 1 | 1.68 | 90 | 183 | 1.51 | 63 | 166 | 89 | 174 |
| 2 | 1.92 | 99 | 194 | 1.73 | 77 | 186 | 100 | 223 |
| 3 | 2.16 | 134 | 231 | 1.94 | 112 | 228 | 150 | 244 |
| 4 | 2.4 | 159 | 256 | 2.16 | 126 | 252 | 153 | 246 |
| 5 | 2.64 | 186 | 279 | 2.38 | 160 | 285 | 199 | 295 |
| 6 | 2.88 | 214 | 304 | 2.59 | 178 | 303 | 210 | 292 |
| 7 | 3.12 | 246 | 329 | 2.81 | 199 | 324 | 286 | 354 |
| 8 | 3.36 | 292 | 363 | 3.02 | 254 | 370 | 365 | 414 |

[a] PEG-4MAL bioink

[b] bis-thiol activator

The average surface roughness $R_a$ for the printed hydrogel matrix was $59.30 \pm 23.81\ \mu m$. The average surface roughness was calculated from the surface heights and depths, measured directly from twenty different experiment images. The surface roughness from the pre-printed hydrogel structure is not controllable, which is caused by the chemical properties of the chosen bioink and activator. The droplet impact on the pre-printed soft hydrogel layer with highly rough surface reflects the real impact process in 3D droplet-based bioprinting method in this study.

## 3.2 Influence of operating conditions on droplet impact

### 3.2.1 Spreading factor

In order to investigate the effect of the bioprinter's operating condition (dosing energy) on the impact dynamics, eight sets of dosing energies listed in Table 2 are conducted. Ink C droplet, as the first droplet that directly impacts on the substrate, has the Weber number ranging from 90 to 292 under 1.68 La to 3.36 La, while the variation of the corresponding Reynolds number ranges from 183 to 363. During the spreading phase of the droplet impact on a flat, dry substrate, the thin liquid lamella bounded by a rim spreads radially. The flow in the spreading droplet is governed mainly by the balance of inertia and viscosity. The velocity of spreading is quickly damped by the viscous stresses (Kittel et al. 2018). The droplet spreads until it reaches the maximum spreading diameter $D_{max}$ (Fig. 6i). The phenomenon of droplet spreading on a soft elastic substrate (Fig. 6ii) is similar to the drop spreading on a dry solid substrate. The maximum spreading diameter was measured directly from the obtained high-speed images.

The spreading factor, as a ratio between the maximum spreading diameter $D_{max}$ and the initial droplet diameter $D_o$, against the Weber number, We, of Ink C impact on two substrates is depicted in Fig. 6. For Ink C, the soft elastic substrate (hydrogel matrix) had generally lower spreading factor than the dry solid substrate (well plate), indicating that soft substrate inhibited the droplet spreading after impact. This is consistent with that proposed by Basso and Bostwick (Basso and Bostwick 2020). The spreading factor of the Ink C/well plate combination showed an increasing trend with the increasing Weber number, while the hydrogel substrate did not have the same increasing tendency. The hydrogel matrix, which can be seen as a thick soft elastic substrate, deformed during droplet impact. The influence of the thick substrate deformation on the rim propagation became significant during spreading when the Weber number is higher than 186.
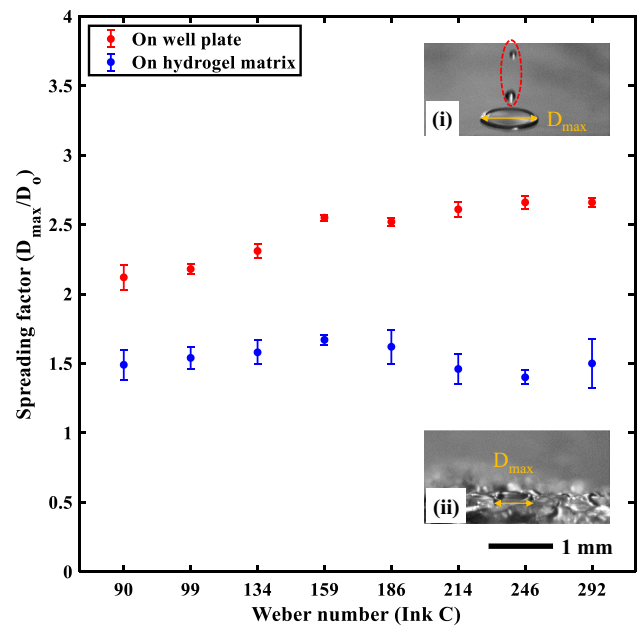


**Fig. 6** Spreading factor, $D_{max}/D_o$, against Weber number, We, for Ink C droplet impacting on the well plate and the hydrogel matrix structure. Example images illustrate the maximum spreading diameter of Ink C droplet impacting on **i** well plate and **ii** hydrogel matrix under We = 134. The satellite droplets generated by droplet formation are circled in red dashed lines. Error bars are 95% confidence intervals

### 3.2.2 General impact phenomena

The simplest observation of droplet impact is whether the drop (1) deposits or (2) splashes on the substrate. This distinction is important as the droplet must impact and leave a single isolated drop to achieve high printing resolution and accuracy. Splashing occurs when the liquid inertia overcomes the surface tension forces, which can be defined as either (1) a drop that produces micro-droplets immediately after impact or (2) a drop that exhibits two or more satellite drops that break off from the main drop during impact (Basso and Bostwick 2020). On the well plate, the Ink C droplets spread to the maximum diameter, then receding back to the equilibrium state. As can be seen at 0 ms in Fig. 7, Ink C left single isolated drops under all dosing energies. Therefore, droplet impact on a dry solid substrate causes no splashing at We ≤ 292, with associated droplet Reynolds number $Re \leq 363$.

When the blank Ink D droplet impacted on the pre-printed Ink C drop, a bowl-like liquid film was generated upon impact at $112 \leq We \leq 254$ and finally receded back to single isolated droplets at around 7.7 s after impingement. The bowl-like liquid film did not break into micro-droplets, but merged during collapse, resulting in entrapment of several bubbles during the contracting phase. The bubbles were gone at the equilibrium state, leaving a single isolated

**Fig. 7** Evolution of the operating conditions on droplet impact. Images were taken from the Side view 2 direction, at 0.2 ms increments (not including the last image), for the blank Ink D droplets impact on the pre-printed Ink C droplets on the well plate. The Weber number of the blank Ink D impact equals to: **i** 63; **ii** 112; **iii** 160; **iv** 199; and **v** 254. The satellite droplets generated by droplet formation are circled in red dashed lines. Scale bar: 1 mm
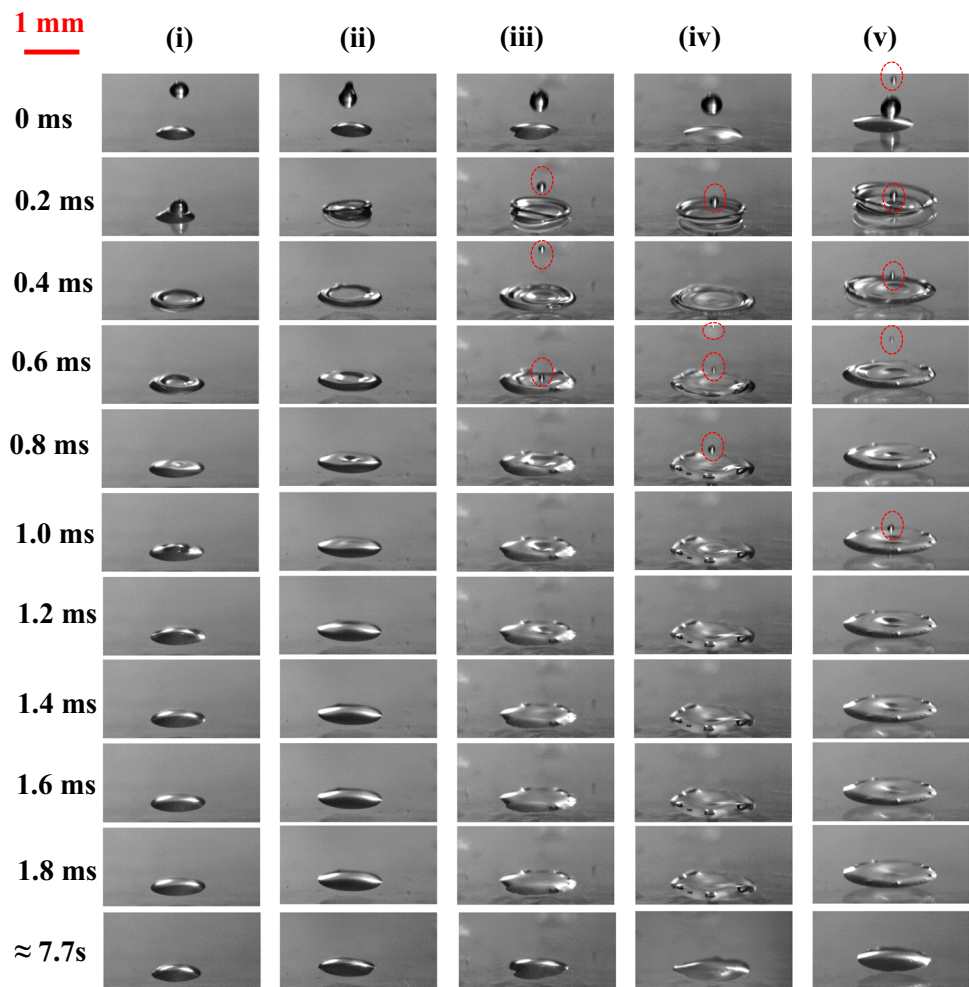


droplet on the substrate. The droplet impact on a wet solid substrate (dimensionless liquid thickness $\delta = h_o/D_o \approx 0.3$) causes no splashing at We $\leq$ 254, with associated droplet Reynolds number $Re \leq$ 370.

Figure 8 shows sequences of droplet impact images on the hydrogel matrix taken from the Side view 2 direction using Ink C under the selected operating conditions (1.68 La, 2.16 La, 2.64 La, 3.12 La, and 3.36 La). The corresponding Weber number values are 90, 134, 186, 246, and 292. On the soft substrate, some of the liquid kinetic energy can be transformed into the elastic energy due to substrate deformation, therefore affecting the impact dynamics and the onset of splashing (Basso and Bostwick 2020). The splashing phenomena on soft substrates was observed at We $\geq$ 186, with associated droplet Reynolds number $Re \geq$ 279. After the spreading phase, an elongated liquid column was formed, followed by the generation of secondary droplets which pinch off from the main droplet. The residual main drop remained on the substrate, which can be seen as the equilibrium droplet for future evaluation. The satellite droplets may rest on the hydrogel substrate, on the wall of the well, or on

the bottom surface of printheads, causing negative effects on printing fidelity. By investigating all dosing energy sets, the splashing phenomena was seen to occur at We = 159, with a splashing percentage (splashing percentage = number of the tests that have splashing phenomenon / total number of the repeat tests under certain Weber number) of 12.9% over the total 31 repeat tests.

The average surface roughness $R_a$ for the printed hydrogel matrix was $59.30 \pm 23.81\ \mu m$. Surface roughness plays an important role in droplet impact on solid substrates. Wang and Qiao (Wang et al. 2021) found that roughness of the solid impact surface ($R_a$ up to 250 $\mu$m) has a positive effect on the dynamics of splashing droplets. Splashing droplet diameter, velocity, splash angle, splash height, and mass-loss rate of splashing droplets rise with the increase in roughness. Quetzeri-Santiago, Miguel A., Alfonso A. Castrejon-Pita, and J. Rafael Castrejon-Pita (Quetzeri-Santiago et al. 2019) also found that the dynamic contact angle, together with the liquid properties, the average surface roughness $R_a$, and the surface feature mean width, determines the splashing to no-splashing threshold in droplet impact process. When

**Fig. 8** Evolution of the operating conditions on droplet impact. Images were taken from the Side view 2 direction, at 0.2 ms increments (not including the last image), for the Ink C droplet impact on the hydrogel matrix with the Weber number equals to: **i** 90; **ii** 134; **iii** 186; **iv** 246; and **v** 292. The satellite droplets generated by droplet formation are circled in red dashed lines. The main droplets are highlighted in yellow dashed lines. Scale bar: 1 mm
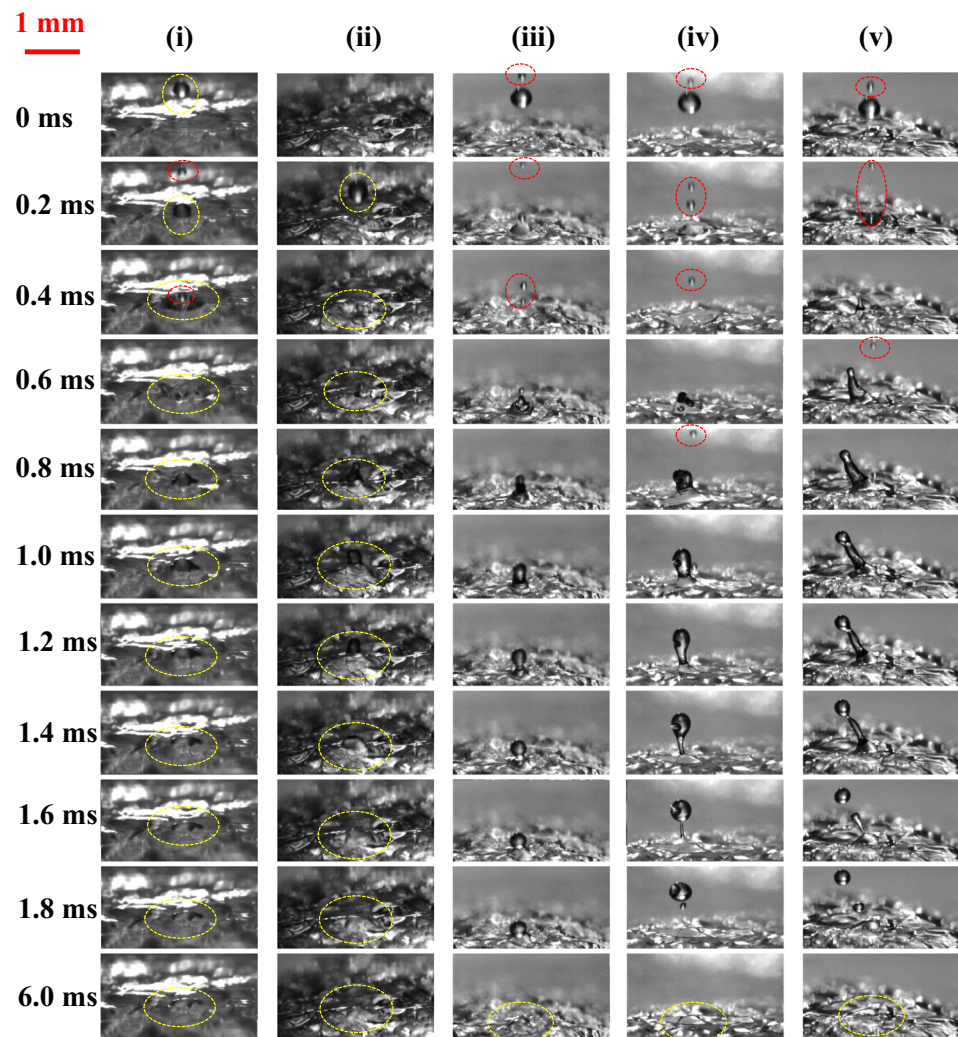


droplets impact on soft matrix, the surface roughness could influence the dynamics of splashing droplets and the splashing threshold. The effects of surface roughness on droplet impact should be discussed in the future work.

Figures 9 and 10 show sequences of images taken from the Side view 2 and the Side view 1, respectively, of blank Ink D droplet impact on the hydrogel matrix with pre-printed Ink C drops on top. The hydrogel matrix covered by pre-printed Ink C drops can be seen as a wet soft substrate. The blank Ink D was shown to be printed under selected operating conditions (1.51 La, 1.94 La, 2.38 La, 2.81 La, and 3.02 La), with the corresponding Weber number equals to 63, 112, 160, 199, and 254. A splashing phenomenon was observed at We ≥ 199 from both viewing directions. By investigating all eight sets of dosing energies, the splashing phenomena started to occur at We = 160, with a splashing percentage of 3.7% over the total 27 repeat tests. Compared with the droplet impact processes on the dry soft substrate, the splashing phenomenon occurs on both dry and wet hydrogel substrates at We > 160. The presence of the pre-printed bioink drop has a negligible influence on splashing.

In the receding phase of droplet impact, droplet retreats after the spreading phase due to the effects of the gelation effect, surface tension of the liquids, surface tension of the substrate, and the interfacial tension between them (Chen et al. 2017). With the hydrogel surface roughness and the gelation effect, the droplet might not retreat evenly. A comparison between the two viewing directions is depicted in Fig. 11. After the blank Ink D droplets impingement on the pre-printed Ink C drops on the well plate, the equilibrium drop diameters were obtained and measured from both viewing directions, at Weber number ranging from 63 to 254. The equilibrium drop diameter increased with increasing Weber number from both viewing directions. The average equilibrium drop diameters obtained from the Side view 1 and the Side view 2 can be seen as consistent, illustrating that the surface roughness or gelation effects has negligible influence on droplet

**Fig. 9** Evolution of the operating conditions on droplet impact. Images were taken from the Side view 2 direction, at 0.2 ms increments (not including the last image), for the blank Ink D droplets impact on the pre-printed Ink C droplets on the hydrogel matrix. The Weber number of the blank Ink D impact equals to: **i** 63; **ii** 112; **iii** 160; **iv** 199; and **v** 254. The satellite droplets generated by droplet formation are circled in red dashed lines. The main droplets are highlighted in yellow dashed lines. Scale bar: 1 mm
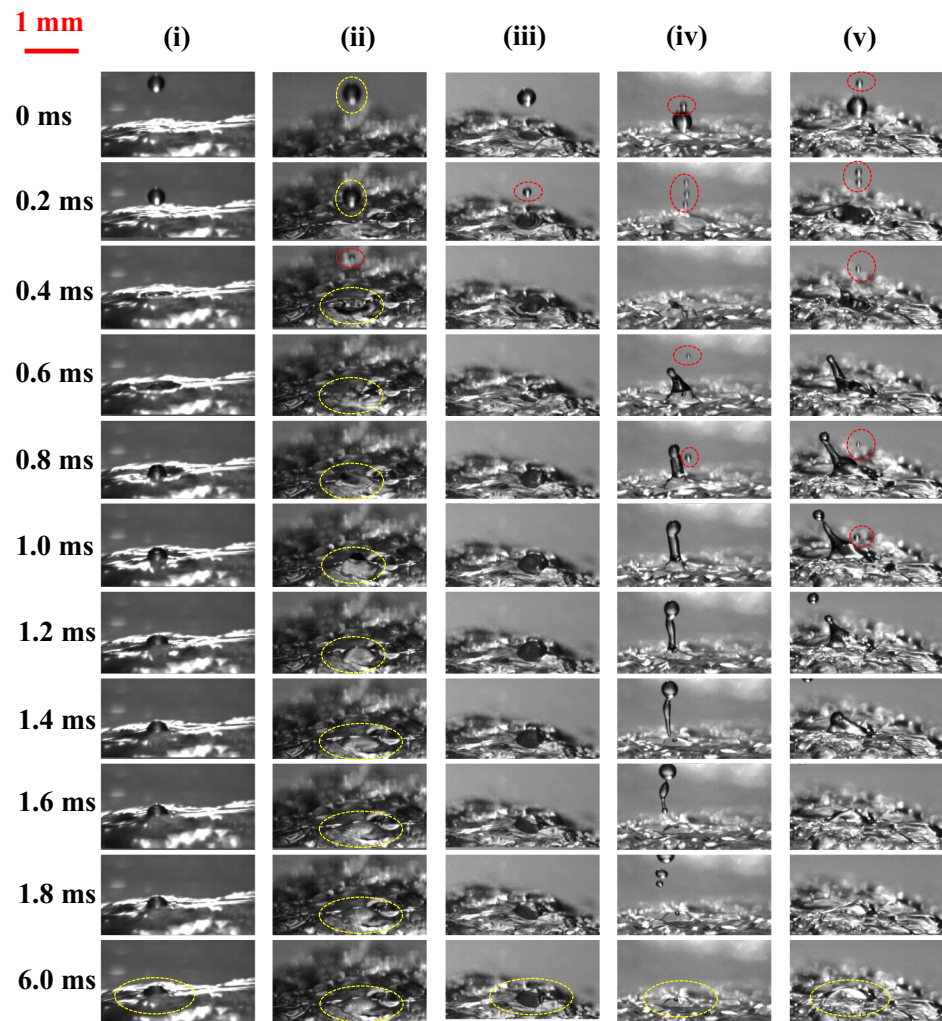


retreat process. Moreover, the viewing direction has negligible effect on the measured drop diameter. Similarly, the equilibrium drop diameters measured after the blank Ink D droplets impinged on the pre-printed Ink C drops on the hydrogel matrix from both viewing directions are very well correlated. Measured values from both viewing directions can be used in future calculations.

An interesting difference between drop impact on the solid surface and the soft structure can be seen in Fig. 11. On the well plate, the equilibrium drop diameter increased with the increasing Weber number. In contrast, the equilibrium drop diameter on the hydrogel matrix started to decrease after We = 160. As discussed before, the splashing phenomenon occurred on soft substrates at We > 160, which can be seen as the main reason causing the decreasing equilibrium droplet size. More results are discussed in the following section.

## 3.3 Influence of substrates on droplet impact

In order to investigate the effect of the substrates on impact dynamics, the general impact processes on the well plate and the hydrogel matrix are presented in Figs. 7, 8, 9, 10. No splashing occurred for We ≤ 292 on both dry and wet solid substrates. With increasing dosing energy, an corresponding increases in Weber number and Reynolds number, droplet spreading diameter and equilibrium diameter increase on both dry and wet solid substrates. The equilibrium drop volume was calculated from the measured equilibrium diameter and height using Eq. 4. The volume increases with the increasing Weber number (Fig. 12). The equilibrium drop volume, after the impact process, increased from 25 ± 7 nl at We = 63 to 93 ± 16 nl at We = 254. Without splashing, the equilibrium droplet volume is as expected for the printed droplet volume generated by the bioprinter.

**Fig. 10** Evolution of the operating conditions on droplet impact. Images were taken from the Side view 1 direction, at 0.2 ms increments (not including the last image), for the blank Ink D droplets impact on the pre-printed Ink C droplets on the hydrogel matrix. The Weber number of blank Ink D impact equals to: **i** 63; **ii** 112; **iii** 160; **iv** 199; and **v** 254. The satellite droplets generated by droplet formation are circled in red dashed lines. The main droplets are highlighted in yellow dashed lines. Scale bar: 1 mm
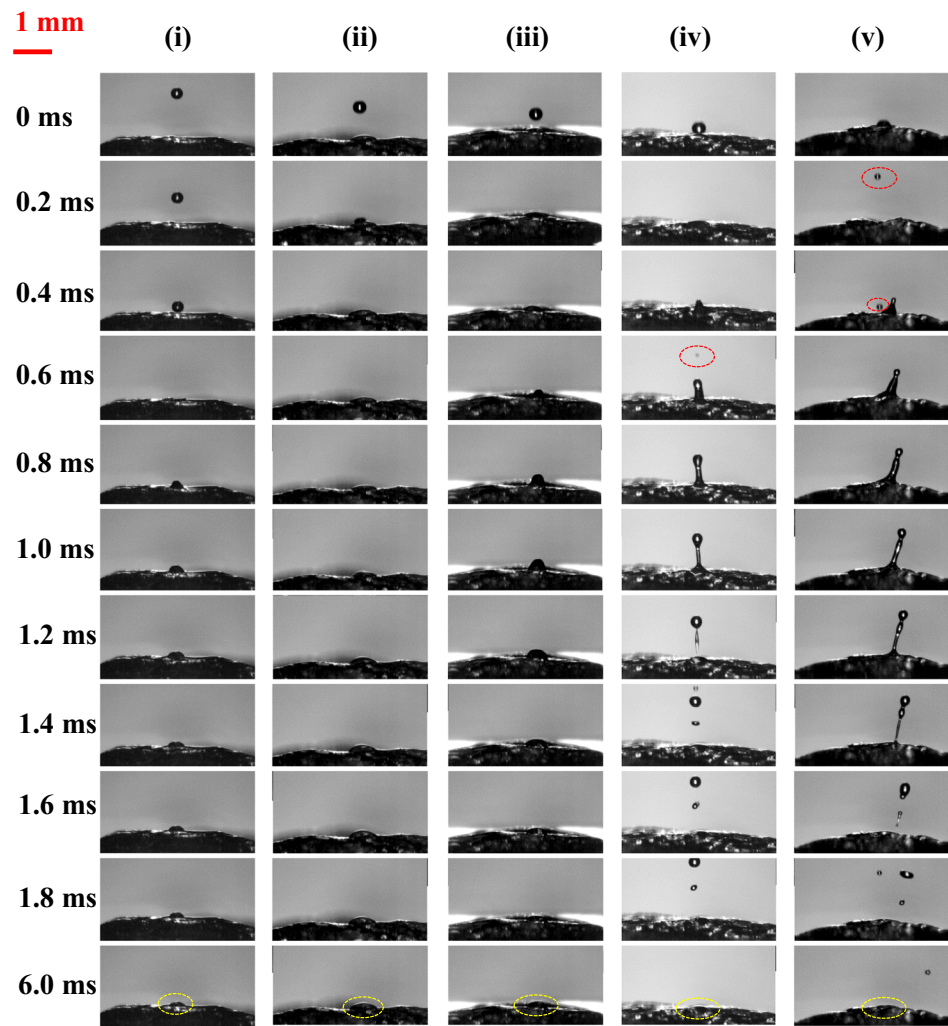


On both the dry and wet soft substrates, splashing was observed for We > 160. The equilibrium drop volume, after the blank Ink D drops impacted on the pre-printed Ink C drops on the hydrogel matrix, increased from 23 ± 5 nl at We = 63 to 43 ± 8 nl at We = 126. At We > 126, the equilibrium drop volume decreased from 30 ± 9 nl at We = 160 to 16 ± 5 nl at We = 254.

At We < 159, with associated Re < 256, the drop collision on the dry soft substrate (Ink C directly impacting on the hydrogel matrix) led to the deposition without breakup. This was also observed for drop impact on the wet soft substrate (blank Ink C impacts on the pre-printed bioink drops on the hydrogel matrix) at We < 127.36, with associated Re < 252. Within this range, the equilibrium drop volume on the soft substrate equalled the total droplet volume applied to the solid substrate. When the Weber number exceeded this value, splashing occurred on the soft substrate. The difference between the equilibrium drop volume on the solid substrate and the droplet size on the soft substrate increased. The printed droplet volume was therefore much lower than the expecting volume, leading to poor printing resolution and reduced structure integrity.

The droplet impact location is another parameter that can directly influence printing fidelity. To investigate the influence of substrates on the droplet impact location, the obtained centre position of the initial droplet before impact was used to compare with the centre position of the equilibrium droplet after impact. On the well plate, the position difference between the initial droplet and the equilibrium droplet was 43.62 ± 18.56 $\mu$m under all applied dosing energies. It is approximately 11% of the droplet diameter. The position difference remained similar after droplet impact on the hydrogel matrix, with a value of 43.10 ± 15.81 $\mu$m under all operating conditions. The splashing has negligible influence on the droplet impact location.

### 3.4 Influence of input cells on droplet impact

Compared to the blank Ink D, the cell-laden Ink D had an increasing density and viscosity, and a decreasing surface
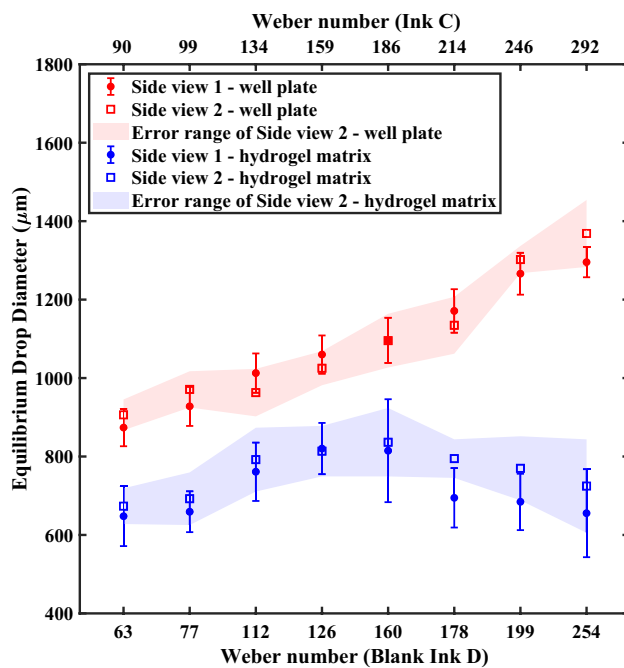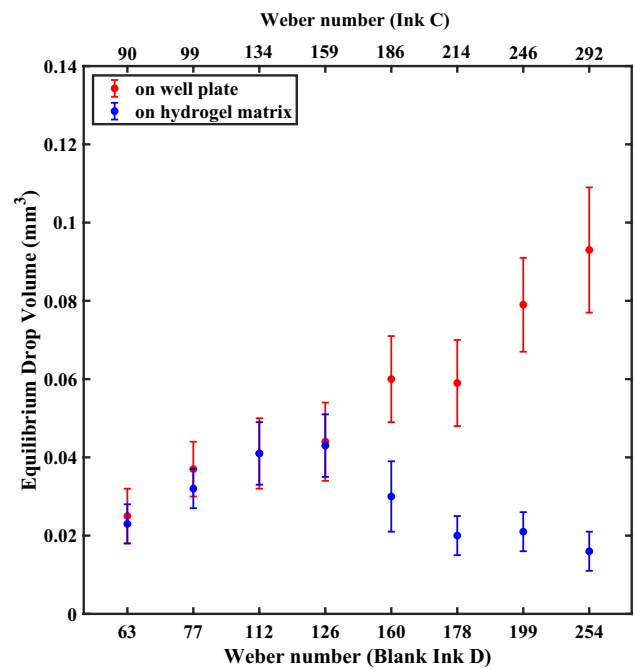
**Fig. 11** The equilibrium drop diameter on the well plate and the hydrogel matrix measured from the Side view 1 and the Side view 2 directions. The Weber number of the first droplet impact (Ink C impacts on the dry substrates) ranges from 90 to 292. The Weber number of the second droplet impact (blank Ink D impacts on the wet substrates) ranges from 63 to 254. Error bars are 95% confidence intervals

**Fig. 12** The calculated equilibrium drop volume on the well plate and hydrogel matrix. The Weber number for the first droplet impact (Ink C impacts on dry substrates) ranges from 90 to 292. The Weber number for the second droplet impact (blank Ink D impacts on wet substrates) ranges from 63 to 254. Error bars are 95% confidence intervals

tension. The initial droplet diameter and falling velocity were not influenced by the amount of input cells in this experiment. The changes in the ink physical properties led to a higher Weber number and Reynolds number upon impact under the same dosing energy. Ink C droplet, which was the first droplet impacting on the soft substrate, had no cells in it. Therefore, the second droplet impact process (the cell-laden Ink D impacts on the pre-printed bioink on the hydrogel matrix) was studied to evaluate the influence of input cells on droplet impact.

The comparison of the equilibrium volume of the blank Ink D Fig. 9 and the cell-laden Ink D Fig. 13 impact on different substrates is depicted in Fig. 14. The average equilibrium drop volume obtained from the blank Ink D and the cell-laden Ink D impact on both solid and soft substrates are very consistent, illustrating the input cell concentration has small effects on the printed drop size.

Fig. 13 shows the evolution of the cell-laden droplet impact process when the Weber number ranges from 89 to 365. At We $\leq$ 153, the cell-laden Ink D impacted on the pre-printed Ink C droplets and combined into single isolated droplets on the soft substrate. Under $E_d = 2.38$La, the corresponding Weber number and Reynolds number of the cell-laden Ink D were calculated to be 199 and 295,

respectively. A splashing phenomenon was observed at this Weber number upon second droplet impact, with a splashing percentage of 75% over the total 12 repeat tests. The blank Ink D showed 3% splashing percentage under the same dosing energy with the associated Weber number equals to 160. The difference in calculated splashing percentage between blank ink and cell-laden ink is mainly caused by the different Weber number. Cell-laden ink has higher Weber number under the same applied dosing energy, where liquid inertia overcomes the surface tension forces, leading splashes to occur.

The total splashing percentage, the first drop splashing percentage, and the second drop splashing percentage under two different cell concentrations (0 and $1 \times 10^7$ cells/ml) can be seen in Fig. 15. First of all, Ink C, which had no cells in it, remained the same under all conditions. The first drop splashing percentage was therefore having the similar value under both tests regardless of the input cell density in Ink D. Ink C started to splash, with an average splashing percentage of 14.78%, on the dry soft hydrogel matrix, at We = 159, with the associated Re = 256. At We = 292, near 100% of Ink C droplets splashed on the soft substrate in droplet impact process. The increasing Weber number leads to an increasing chance of droplet splashing on the soft substrate.

**Fig. 13** Evolution of $1 \times 10^7$ cells/ml input cell concentration on droplet impact. Images were taken from the Side view 2 direction, at 0.2 ms increments (not including the last image), for the cell-laden Ink D droplets impact on the pre-printed Ink C droplets on the hydrogel matrix. The Weber number of the cell-laden Ink D droplets impact equals to: **i** 89; **ii** 150; **iii** 199; **iv** 286; and **v** 365. Scale bar: 1 mm
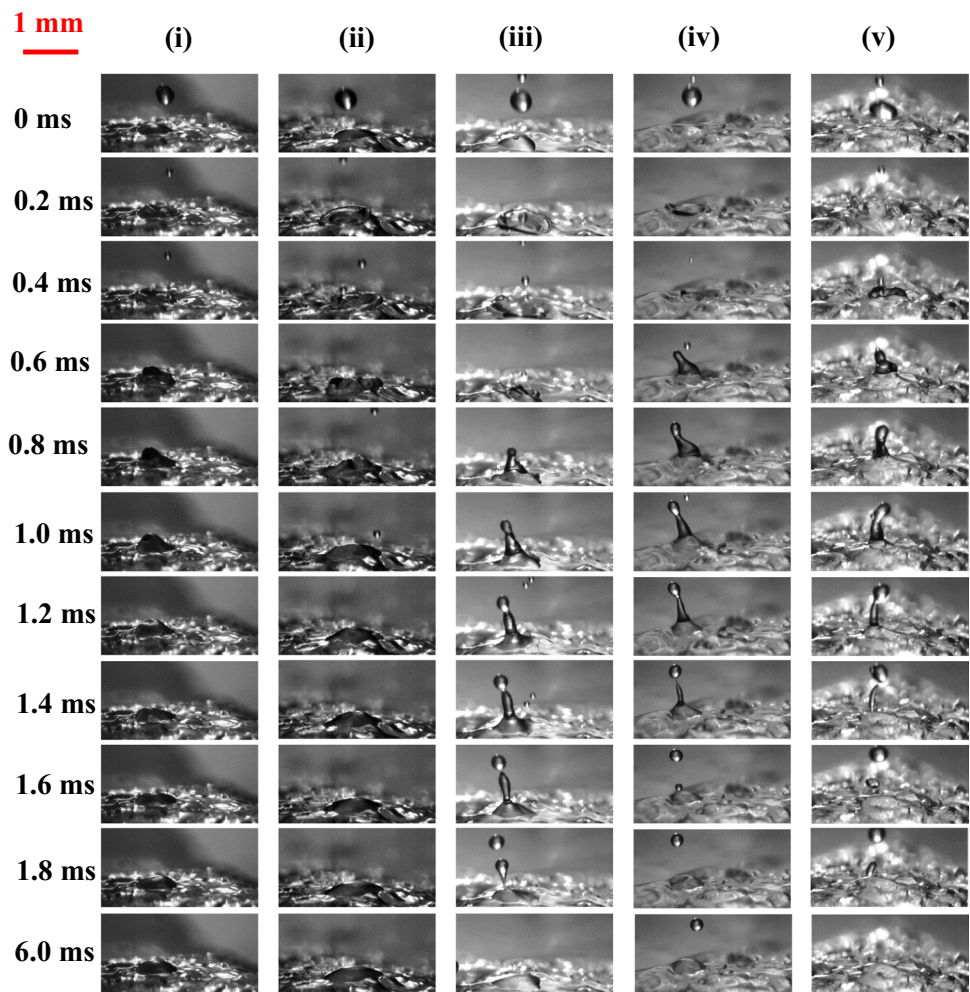


When a blank Ink D droplet was printed on top of the pre-printed Ink C, there was no splashing at We $\leq$ 126, with associated Re $\leq$ 252. Under 2.38$La$, where the blank Ink D has a Weber number of 160, 3% of the blank Ink D splashed on the pre-printed bioink, on top of the soft hydrogel matrix. The splashing percentage for the blank Ink D increased to 41.46% under 2.59La(We = 178), to 39.29% under 2.81La(We = 199), to 48.28% under 3.02La(We = 254). The cell-laden Ink D, on the other hand, illustrated much higher splashing rate under the same applied dosing energies due to its large Weber number. Similar to the blank Ink D, no splashing was generated under 2.16 $La$. When the applied dosing energy increased to 2.38$La$, the Weber number of the cell-laden Ink D raised to 199, resulting 75% splashing percentage. The splashing percentage of the cell-laden Ink D kept increasing to 78.26% under 2.59La(We = 210), up to near 100% under 3.02La(We = 365).

### 3.5 Splashing threshold

Mundo et al. (Mundo et al. 1995) have suggested the dimensionless number $K = \mathrm{We}^{0.5}\mathrm{Re}^{0.25}$ as an effective metric to quantify splashing. In addition to the $K$ number, Kittel et al. (Kittel et al. 2018) surmised that the splashing condition for drop impact onto soft, deformable substrates can be obtained from the balance of the inertial and surface tension forces in the spreading lamella. The threshold value $L$ is defined by the ratio of the pressure associated with the liquid inertia ($p_i = \mathrm{rho} v_o^2$) and the capillary pressure on the length scale associated with the residual lamella thickness ($p_\sigma = \frac{\sigma}{D_o \mathrm{Re}^{-2/5}}$) (Kittel et al. 2018).

$$L = \frac{p_i}{p_\sigma} = \mathrm{We}\mathrm{Re}^{-0.4} \tag{7}$$
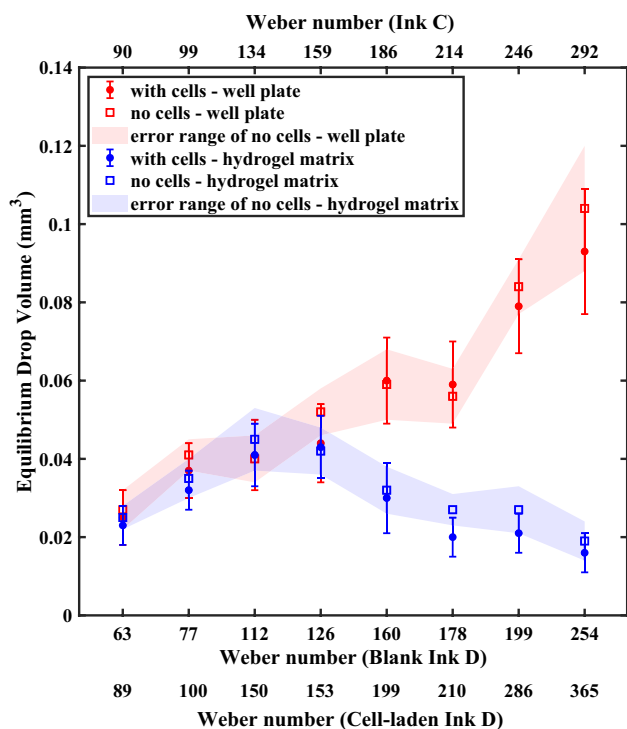
**Fig. 14** The calculated equilibrium drop volume on the well plate and hydrogel matrix under different input cell concentration (0 and $1 \times 10^7$ cells/ml). The Weber number for the first droplet impact (Ink C impacts on dry substrates) ranges from 90 to 292. The Weber number for the second droplet impact (blank Ink D impacts on wet substrates) ranges from 63 to 254. The Weber number for the second droplet impact (cell-laden Ink D impacts on wet substrates) ranges from 89 to 365. Error bars are 95% confidence intervals

The K number and L number of the inks under eight sets of bioprinter's operating conditions for Ink C and blank/cell-laden Ink D are listed in Table. 3. Three phases can be used to describe the 3D-bioprinted droplet impact process on the pre-printed soft hydrogel matrix: (1) Droplet deposition/no splashing, where the total splashing percentage is 0%; (2) Partial splashing, where the splashing occurs, while the total splashing percentage is lower than 100%; and (3) Absolute splashing, where the total splashing percentage equals to 100%.

On both dry and wet flat solid substrate, no splashing happened under the tested operating conditions, regardless of input cell densities. The splashing threshold for the droplet impact on dry and wet solid substrate is defined by $K < 86.19$. This threshold is consistent with the results ($K = 84$) reported by Kittel et al.(Kittel et al. 2018).

Ink C started to splash on the dry soft hydrogel matrix, at We = 159, with the associated Re = 256. To define splashing for Ink C on a thick soft substrate, the critical $K$ and $L$ number is 45.11 and 15.21, respectively, calculated from the experimental results with corresponding We = 134 and Re = 231. At We = 292 and Re = 363, nearly 100% of Ink C droplets splashed on the soft substrate. The $K$ and $L$ number that defines the absolute splashing threshold for Ink C are therefore set as 74.53 and 27.61, respectively. The partial splashing phase of Ink C on thick soft hydrogel substrate is bound by these two threshold limiting values.

The blank Ink D started to splash on the wet soft hydrogel matrix, at We = 160, with the corresponding Reynolds number, $K$ number, and $L$ number as Re = 285, $K$ = 52.03,
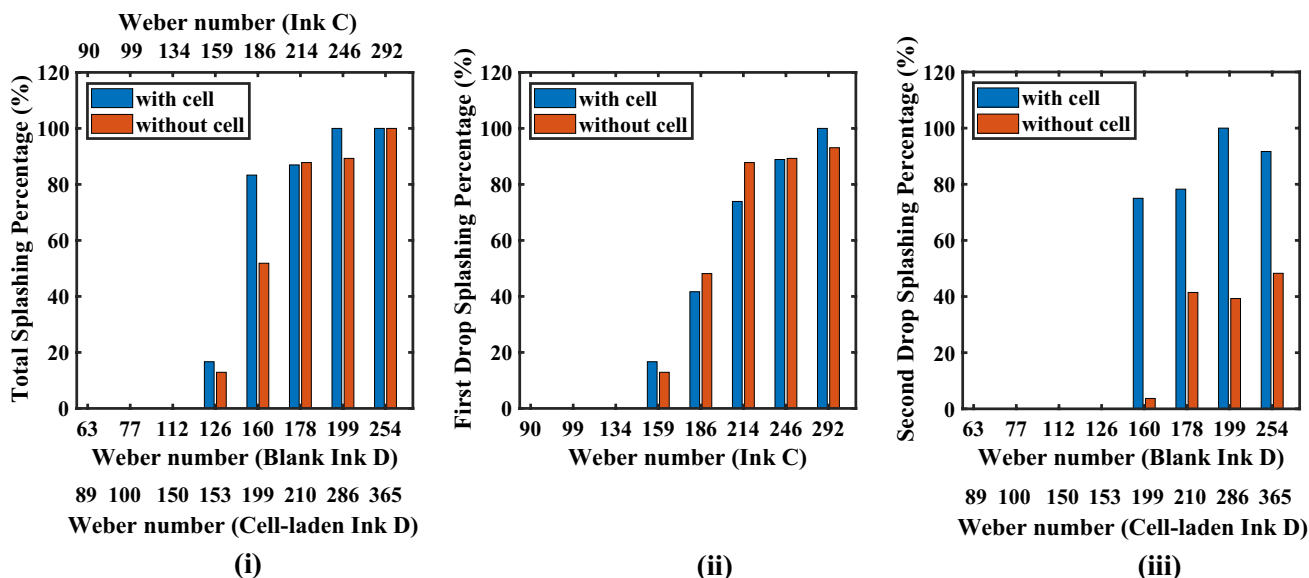


**Fig. 15** Splashing percentage under two different cell concentrations (0 and $1 \times 10^7$ cells/ml): **i** The total splashing percentage: including both the first droplet impact and the second droplet impact; **ii** The first drop splashing percentage; **iii** The second drop splashing percentage

**Table 3** Weber number, We, Reynolds number, Re, $K$ number, and $L$ number of the inks under eight sets of bioprinter's operating conditions

| | Ink C[a] | | | | Ink D[b] seeded with 0 cells/ml cells | | | | Ink D seeded with $1 \times 10^7$ cells/ml cells | | | |
|---|---|---|---|---|---|---|---|---|---|---|---|---|
| Set | We | Re | K | L | We | Re | K | L | We | Re | K | L |
| 1 | 90 | 183 | 34.88 | 11.20 | 63 | 166 | 28.54 | 8.17 | 89 | 174 | 34.21 | 11.25 |
| 2 | 99 | 194 | 37.05 | 12.00 | 77 | 186 | 32.49 | 9.58 | 100 | 223 | 37.15 | 12.23 |
| 3 | 134 | 231 | 45.11 | 15.21 | 112 | 228 | 41.02 | 12.73 | 150 | 244 | 48.38 | 16.61 |
| 4 | 159 | 256 | 50.51 | 17.35 | 126 | 252 | 44.78 | 13.85 | 153 | 246 | 48.98 | 16.94 |
| 5 | 186 | 279 | 55.75 | 19.54 | 160 | 285 | 52.03 | 16.74 | 199 | 295 | 58.45 | 20.44 |
| 6 | 214 | 304 | 61.03 | 21.71 | 178 | 303 | 55.67 | 18.13 | 210 | 292 | 59.82 | 21.64 |
| 7 | 246 | 329 | 66.82 | 24.26 | 199 | 324 | 59.78 | 19.66 | 286 | 354 | 73.41 | 27.36 |
| 8 | 292 | 363 | 74.53 | 27.61 | 254 | 370 | 69.97 | 23.87 | 365 | 414 | 86.19 | 32.81 |

[a]PEG-4MAL bioink

[b]bis-thiol activator

and $L = 16.74$. To prevent splashing, the deposition/splashing boundary for the blank Ink D on thick soft substrate should be lower than these values, which are set to be $K = 44.78$ and $L = 13.85$ based on the experimental results. At We $= 254$ and Re $= 370$, the total splashing percentage for the blank Ink D impacting on the wet hydrogel substrate reached to 100%. The absolute splashing happens at $K = 69.97$ and $L = 23.87$. The partial splashing phase of the blank Ink C on wet thick soft substrate is bound by these two threshold limiting values.

Similarly, the cell-laden Ink D started to splash on the wet soft hydrogel matrix, at We $= 199$, with the corresponding Reynolds number, $K$ number, and $L$ number as Re $= 295$, $K = 58.45$, and $L = 20.44$. To prevent splashing, the deposition/splashing boundary for the cell-laden Ink D on thick soft substrate should be lower than these values, which are set to be $K = 48.98$ and $L = 16.94$ based on the experimental results. At We $= 286$ and Re $= 354$, the total splashing percentage for the cell-laden Ink D impacting on the wet hydrogel substrate reached to 100%. The absolute splashing happens at $K = 73.41$ and $L = 27.36$. The partial splashing phase of the blank Ink C on wet thick soft substrate is bounded by these two threshold limiting values.
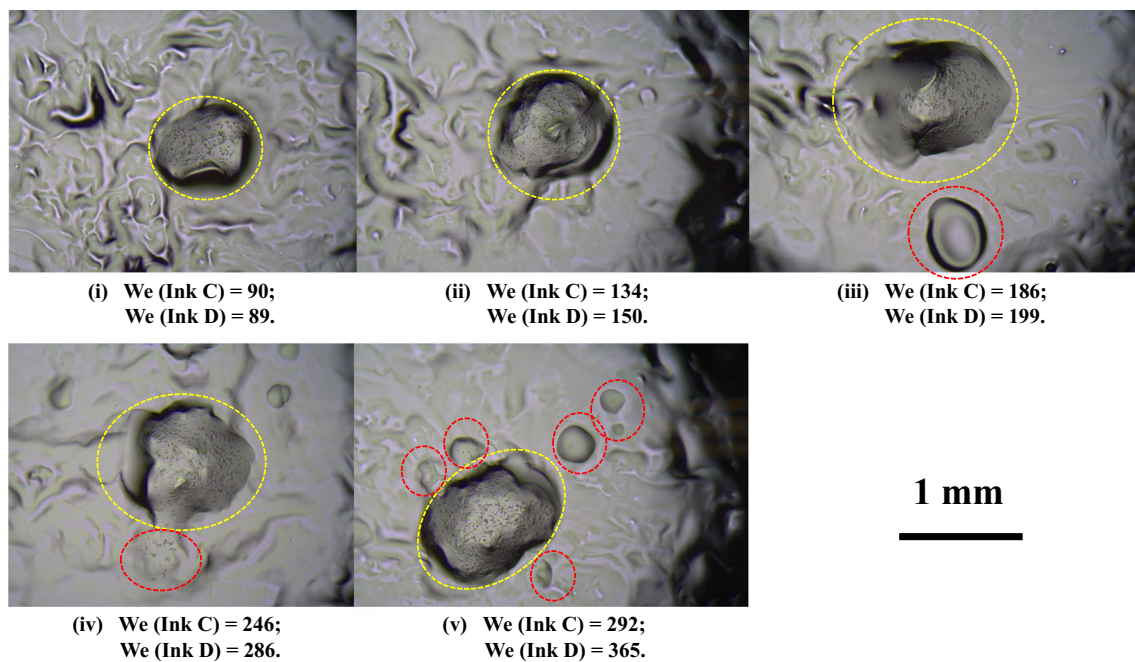
Combining the threshold values for all types of ink, input cell densities, and substrate conditions (dry or wet), the deposition/splashing boundary for both the dry and wet soft hydrogel matrix is defined as $K = 44.78$ and $L = 13.85$. The obtained threshold ranges are in agreement with the existing recent theories for splashing threshold ($K = 57.7$, (Mundo et al. 1995, Ng et al. 2022) $K < 175$, (Basso and Bostwick 2020) and $L = 16.8$. (Kittel et al. 2018)) on soft substrates. The threshold for absolute splashing is defined as $K = 73.41$ and $L = 27.36$. The partial splashing phase is bounded between these two values. This combined threshold should be able to use to achieve high printing fidelity and structure integrity.

## 3.6 Droplet impact influence on bioprinted 3D cell spheroids

Three droplet impact phases (droplet deposit/no splashing, partial splashing, and absolute splashing) on hydrogel matrix have been identified in this study. Figs. 16, 17 are used to illustrate how different droplet impact phases influence the printing outcomes within the droplet-based 3D bioprinting process.

Bright-field images were obtained right after the droplet impact experiment. At We $\leq 154$, both bioink droplets and activator droplets were deposited on the pre-printed hydrogel matrix to form isolated single hydrogel drops. Fig. 16i and ii demonstrates the isolated hydrogel droplets after depositing cell-laden activator Ink D on top of the pre-printed bioink Ink C. The isolated hydrogel droplets indicate potential good outcome for 3D cell spheroids generation. At We $> 154$, droplets started to splash on the soft substrate upon impact. The satellite drops caused by splashing around the main hydrogel droplet can be seen in Fig. 16iii, iv and v. Cells that trapped in the satellite drops could not bound with bioink, resulting in extra cells floating in the cell culture media and contaminating the culturing field. Moreover, when a large amount of bioink (Ink C) splashed during impact process (Fig. 16iii), there was not enough bioink left in the main droplet for a good gelation after. The formation of 3D cell spheroids will be negatively influenced.

After 7 days incubation, the fluorescence images of generated 3D cell spheroids can be seen in Fig. 17. Compared to the deposition/no splashing printing results (Fig. 17i, ii, iii, and v), the satellite drops caused by splashing resulted inconsistent printing results. In the absence of splashing, the printed cells formed into isolated spherical structures, which can be used in future experiments. In contrast, the cell-laden droplets that went through splashing did not form into the ideal 3D cell spheroids and cannot be used in the future.

**(i) We (Ink C) = 90;**
**We (Ink D) = 89.**

**(ii) We (Ink C) = 134;**
**We (Ink D) = 150.**

**(iii) We (Ink C) = 186;**
**We (Ink D) = 199.**

**(iv) We (Ink C) = 246;**
**We (Ink D) = 286.**

**(v) We (Ink C) = 292;**
**We (Ink D) = 365.**

**1 mm**

**Fig. 16** Bright-field images of the cell-laden activator Ink D impacts on the bioink Ink D on the top of the hydrogel matrix, at the Weber number of the cell-laden Ink D equals to: **i** 89 (no splashing); **ii** 150 (no splashing); **iii** 199 (partial splashing); **iv** 286 (absolute splashing); and **v** 365 (absolute splashing). The satellite droplets generated by splashing are circled by red dashed lines. The main droplets are highlighted by yellow dashed lines

## 4 Conclusion

Droplet splashing on pre-printed soft hydrogel substrate has been experimentally investigated using a micro-valve-based 3D bioprinter under different conditions. Droplet impact dynamics was captured by the shadowgraphy method using a high-speed imaging system. The droplet volume, falling velocity, and impact morphology were obtained by analysis of processed images from the camera. The droplet impact morphology was quantified by the spreading factor, Weber number, We, Reynolds number, Re, splashing percentage, and the threshold number $K$ and $L$. For droplet spreading, the soft substrate can inhibit the spreading after impact. The influence of the thick substrate deformation on the rim propagation became significant during spreading when the Weber number is higher than 186, which inhibit the droplet spreading during impact more. Kittel (Kittel et al. 2018) summarised the splashing threshold $K$ number for droplet impact on flat surfaces smaller than 84. In this experiment, droplet impact on a dry/wet solid substrate causes no splashing with $K$ number up to 86.19.
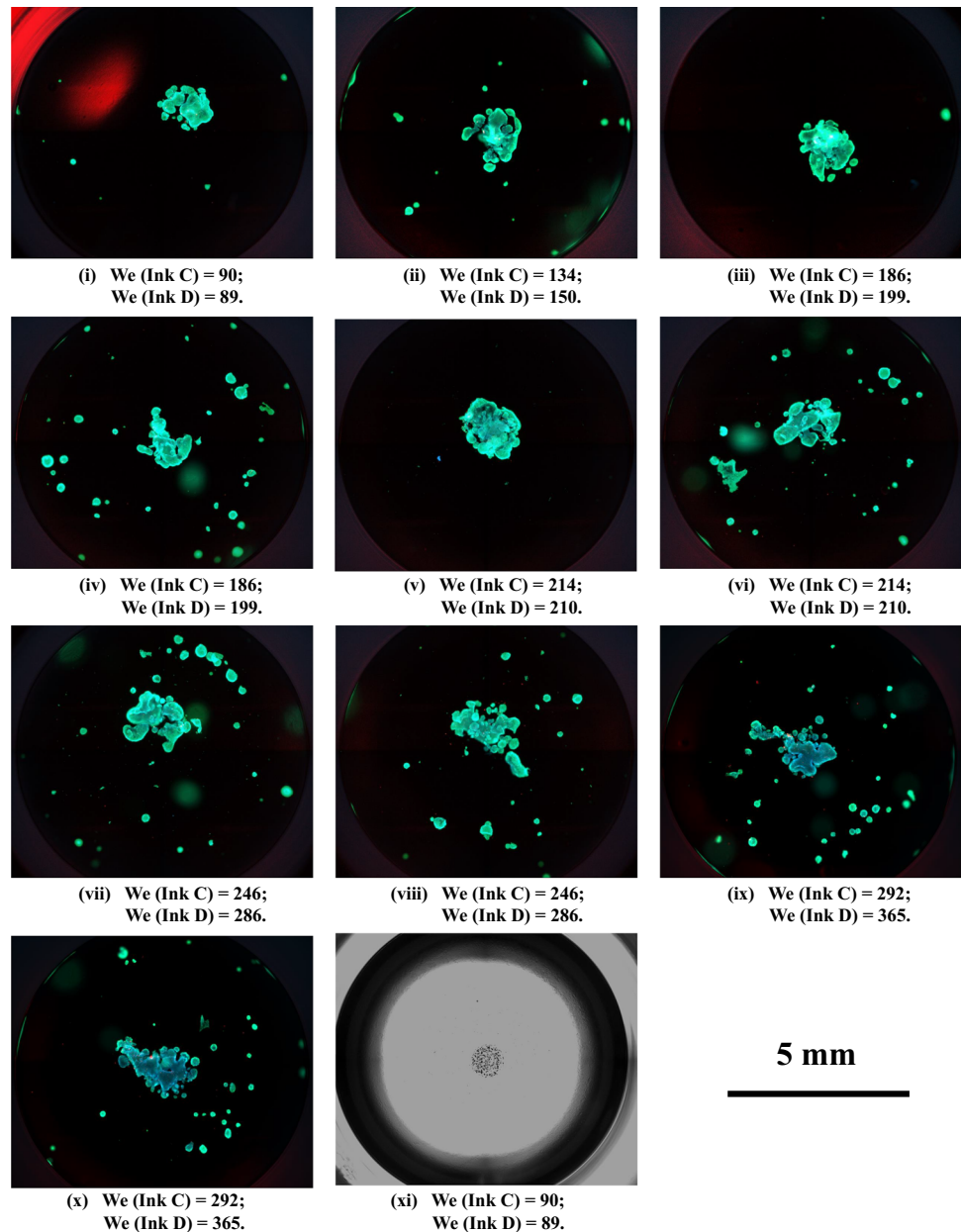
Three phases was used to describe the droplet impact process on thick soft hydrogel matrix: (1) Droplet deposition/no splashing, where the total splashing percentage is 0%; (2) Partial splashing, where the splashing occurs, while the total splashing percentage is lower than 100%; and (3) Absolute splashing, where the total splashing percentage equals to 100%.

The deposition/splashing threshold for droplet impact on both the dry and wet soft hydrogel matrix is defined as $K = 44.78$ and $L = 13.85$, regardless of ink property or input cell density. The obtained threshold ranges are in agreement with the existing recent theories for splashing threshold ($K = 57.7$ and $L = 16.8$) (Basso and Bostwick 2020, Kittel et al. 2018) on soft substrates. Beyond the threshold, the printed drop volume will be much lower than the expected volume due to splashing, leading to poor printing fidelity and structural integrity. The absolute splashing threshold for the dry and wet soft hydrogel matrix is defined as $K = 73.41$ and $L = 27.36$. The partial splashing phase is bounded between these values. No dependency of the input cell density was observed once the threshold was overcome. Droplet splashing on the soft substrate during impact could significantly influence the printed 3D cell structural accuracy and integrity in 3D bioprinting processes. However, splashing has proven to have negligible influence on the droplet impact location.

Our work provides new insights into droplet deposition and fusion in droplet-based 3D bioprinting. The optimization of printing condition based on the splashing thresholds will aid in achieving high printing fidelity and maintain structure integrity. Future work includes discussing the effects of surface roughness of soft hydrogel matrix

**Fig. 17** Fluorescence images of 3D cell spheroids generated under different operating conditions, with the corresponding Weber number of the cell-laden Ink D equals to: **i** 89 (no splashing); **ii** 150 (no splashing); **iii** 199 (partial splashing - no splashing); **iv** 199 (partial splashing - splashing); **v**) 210 (partial splashing - no splashing); **vi** 210 (partial splashing - splashing); **vii** 286 (absolute splashing); **viii** 286 (absolute splashing); **ix** 365 (absolute splashing); **x** 365 (absolute splashing); **xi** 89 (Control set: 2D cell structure, no splashing)



(i) We (Ink C) = 90; We (Ink D) = 89.

(ii) We (Ink C) = 134; We (Ink D) = 150.

(iii) We (Ink C) = 186; We (Ink D) = 199.

(iv) We (Ink C) = 186; We (Ink D) = 199.

(v) We (Ink C) = 214; We (Ink D) = 210.

(vi) We (Ink C) = 214; We (Ink D) = 210.

(vii) We (Ink C) = 246; We (Ink D) = 286.

(viii) We (Ink C) = 246; We (Ink D) = 286.

(ix) We (Ink C) = 292; We (Ink D) = 365.

(x) We (Ink C) = 292; We (Ink D) = 365.

(xi) We (Ink C) = 90; We (Ink D) = 89.

5 mm

on the dynamics of splashing droplets and the splashing threshold.

**Data availability** The data that support the findings of this study are available from the corresponding author upon reasonable request.

## Declarations

**Conflict of interest:** Not applicable

**Ethics approval** Not applicable

# References

Murphy SV, Atala A (2014) 3D bioprinting of tissues and organs. Nat Biotechnol 32(8):773–785. https://doi.org/10.1038/nbt.2958

Derakhshanfar S, Mbeleck R, Xu K, Zhang X, Zhong W, Xing M (2018) 3d bioprinting for biomedical devices and tissue engineering: a review of recent trends and advances. Bioact Mater 3(2):144–156. https://doi.org/10.1016/j.bioactmat.2017.11.008

Chameettachal S, Yeleswarapu S, Sasikumar S, Shukla P, Hibare P, Bera AK, Bojedla SSR, Pati F (2019) 3D Bioprinting: recent trends and challenges. J Indian Inst Sci 99(3):375–403. https://doi.org/10.1007/s41745-019-00113-z

Mobaraki M, Ghaffari M, Yazdanpanah A, Luo Y, Mills DK (2020) Bioinks and bioprinting: a focused review. Bioprinting. https://doi.org/10.1016/j.bprint.2020.e00080

Vanaei S, Parizi MS, Vanaei S, Salemizadehparizi F, Vanaei HR (2021) An overview on materials and techniques in 3D bioprinting toward biomedical application. Eng Regen 2:1–18. https://doi.org/10.1016/j.engreg.2020.12.001

Gudapati H, Dey M, Ozbolat I (2016) A comprehensive review on droplet-based bioprinting: past, present and future. Biomaterials 102:20–42. https://doi.org/10.1016/j.biomaterials.2016.06.012

Saygili E, Dogan-Gurbuz AA, Yesil-Celiktas O, Draz MS (2020) 3D bioprinting: a powerful tool to leverage tissue engineering and microbial systems. Bioprinting 18:00071. https://doi.org/10.1016/j.bprint.2019.e00071

Machekposhti SA, Movahed S, Narayan RJ (2020) Physicochemical parameters that underlie inkjet printing for medical applications. Biophys Rev 1(1):011301. https://doi.org/10.1063/5.0011924

Li X, Liu B, Pei B, Chen J, Zhou D, Peng J, Zhang X, Jia W, Xu T (2020) Inkjet bioprinting of biomaterials. Chem Rev 120(19):10793–10833. https://doi.org/10.1021/ACS.CHEMREV.0C00008

Bejoy AM, Makkithaya KN, Hunakunti BB, Hegde A, Krishnamurthy K, Sarkar A, Lobo CF, Keshav DVS, Dharshini G, Mascarenhas S, Chakrabarti S, Kalepu SRRD, Paul B, Mazumder N (2021) An insight on advances and applications of 3d bioprinting: a review. Bioprinting 24:00176. https://doi.org/10.1016/j.bprint.2021.e00176

Ouyang L, Yao R, Zhao Y, Sun W (2016) Effect of bioink properties on printability and cell viability for 3D bioplotting of embryonic stem cells. Biofabrication 8(3):035020. https://doi.org/10.1088/1758-5090/8/3/035020

Ng WL, Lee JM, Yeong WY, Win Naing M (2017) Microvalve-based bioprinting-process, bio-inks and applications. Biomater Sci 5(4):632–647. https://doi.org/10.1039/c6bm00861e

Xu H, Casillas J, Xu C (2019) Effects of printing conditions on cell distribution within microspheres during inkjet-based bioprinting. AIP Adv. https://doi.org/10.1063/1.5116371

Ng WL, Lee JM, Zhou M, Chen YW, Lee KXA, Yeong WY, Shen YF (2020) Vat polymerization-based bioprinting - process, materials, applications and regulatory challenges. Biofabrication 12(2):022001. https://doi.org/10.1088/1758-5090/ab6034

Zhang Y, Kumar P, Lv S, Xiong D, Zhao H, Cai Z, Zhao X (2021) Recent advances in 3D bioprinting of vascularized tissues. Mater Des 199:109398. https://doi.org/10.1016/j.matdes.2020.109398

Yilmaz B, Al Rashid A, Mou YA, Evis Z, Koç M (2021) Bioprinting: a review of processes, materials and applications. Bioprinting 23:00148. https://doi.org/10.1016/j.bprint.2021.e00148

Liu Y, Derby B (2019) Experimental study of the parameters for stable drop-on-demand inkjet performance. Phys Fluids 31(3):032004. https://doi.org/10.1063/1.5085868

Derby B (2010) Inkjet printing of functional and structural materials: fluid property requirements, feature stability, and resolution. Annu Rev Mater Res 40(1):395–414. https://doi.org/10.1146/annurev-matsci-070909-104502

Gong Y, Bi Z, Bian X, Ge A, He J, Li W, Shao H, Chen G, Zhang X (2020) Study on linear bio-structure print process based on alginate bio-ink in 3D bio-fabrication. Bio-Des Manuf 3(2):109–121. https://doi.org/10.1007/s42242-020-00065-9

Yarin AL et al (2006) Drop impact dynamics: splashing, spreading, receding, bouncing. Annu Rev Fluid Mech 38(1):159–192

Mao T, Kuhn DC, Tran H (1997) Spread and rebound of liquid droplets upon impact on flat surfaces. AIChE J 43(9):2169–2179

Weiss DA, Yarin AL (1999) Single drop impact onto liquid films: neck distortion, jetting, tiny bubble entrainment, and crown formation. J Fluid Mech 385:229–254

Howland CJ, Antkowiak A, Castrejón-Pita JR, Howison SD, Oliver JM, Style RW, Castrejón-Pita AA (2016) It's harder to splash on soft solids. Phys Rev Lett 117:184502. https://doi.org/10.1103/PhysRevLett.117.184502

Ng WL, Huang X, Shkolnikov V, Goh GL, Suntornnond R, Yeong WY (2022) Controlling droplet impact velocity and droplet volume: key factors to achieving high cell viability in sub-nanoliter droplet-based bioprinting. Int J Bioprinting 8:1–17. https://doi.org/10.18063/IJB.V8I1.424

Basso BC, Bostwick JB (2020) Splashing on soft elastic substrates. Langmuir 36(49):15010–15017. https://doi.org/10.1021/acs.langmuir.0c02500

Saile D, Kühl V, & Gülhan A (2019) On the subsonic near-wake of a space launcher configuration without exhaust jet. Experiments inFluids 60(50):1–17.

Saile D, Kühl V, Gülhan A (2019) On the subsonic near-wake of a space launcher configuration with exhaust jet. Experiments inFluids 60(165):1–17

Unagolla JM, Jayasuriya AC (2020) Hydrogel-based 3D bioprinting: a comprehensive review on cell-laden hydrogels, bioink formulations, and future perspectives. Appl Mater Today 18:100479. https://doi.org/10.1016/J.APMT.2019.100479

Catros S, Guillotin B, Bačáková M, Fricain J-C, Guillemot F (2011) Effect of laser energy, substrate film thickness and bioink viscosity on viability of endothelial cells printed by laser-assisted bioprinting. Appl Surf Sci 257(12):5142–5147

Utama RH, Tan VTG, Tjandra KC, Sexton A, Nguyen DHT, O'Mahony AP, Du EY, Tian P, Ribeiro JCC, Kavallaris M, Gooding JJ (2021) A covalently crosslinked ink for multimaterials drop-on-demand 3D bioprinting of 3D cell cultures. Macromol Biosci 21(9):2100125. https://doi.org/10.1002/mabi.202100125

Utama RH, Atapattu L, O'Mahony AP, Fife CM, Baek J, Allard T, O'Mahony KJ, Ribeiro J, Gaus K, Kavallaris M, Gooding J (2020) Precise, high-throughput production of multicellular spheroids with a bespoke 3D bioprinter. bioRxiv. https://doi.org/10.1101/2020.04.06.028548

Arashiro EY, Demarquette NR (1999) Use of the pendant drop method to measure interfacial tension between molten polymers. Mater Res 2(1):23–32. https://doi.org/10.1590/S1516-14391999000100005

Berry JD, Neeson MJ, Dagastine RR, Chan DYC, Tabor RF (2015) Measurement of surface and interfacial tension using pendant drop tensiometry. J Colloid Interface Sci 454:226–237. https://doi.org/10.1016/J.JCIS.2015.05.012

Klinger M, Laske C, Graeve M, Thoma M, Traube A (2020) A Sensor for the In-Flight Detection of Single Fluorescent Microbodies in Nanoliter Droplets. IEEE Sens J 20(11):5809–5817. https://doi.org/10.1109/JSEN.2020.2972268

Chen X, O'Mahony AP, Barber T (2021) The characterization of particle number and distribution inside in-flight 3D printed droplets using a high speed droplet imaging system. J Appl Phys 130(4):044701. https://doi.org/10.1063/5.0058817/5.0058817.MM.ORIGINAL.V10.MP4

Chen X, O'Mahony AP, Barber T (2022) The assessment of average cell number inside in-flight 3D printed droplets in microvalve-based bioprinting. J Appl Phys 131(22):224701. https://doi.org/10.1063/5.0096468

Engel M, Belfiore L, Aghaei B, Sutija M (2022) Enabling high throughput drug discovery in 3D cell cultures through a novel bioprinting workflow. SLAS Technol 27(1):32–38. https://doi.org/10.1016/J.SLAST.2021.10.002

Mallinson S, Barber T, Yeoh G, McBain G (2018) Simulation of droplet impact and spreading using a simple dynamic contact angle model. SIMULATION 10:13

Kang SH, Kim S, Sohn DK, Ko HS (2020) Analysis of drop-on-demand piezo inkjet performance. Phys Fluids 32(2):022007. https://doi.org/10.1063/1.5142023

Xu C, Zhang M, Huang Y, Ogale A, Fu J, Markwald RR (2014) Study of droplet formation process during drop-on-demand inkjetting of living cell-laden bioink. Langmuir 30(30):9130–9138. https://doi.org/10.1021/la501430x

Ng WL, Yeong WY, Naing MW (2017) Polyvinylpyrrolidone-based bio-ink improves cell viability and homogeneity during drop-on-demand printing. Materials. https://doi.org/10.3390/ma10020190

Mahmodi H, Piloni A, Utama RH, Kabakova I (2021) Mechanical mapping of bioprinted hydrogel models by brillouin microscopy. Bioprinting 23:00151

Wang Q, Lin X, Lin Y, Ma J, Xiao J, Wu Y, Wang J (2021) Effects of surface roughness on splashing characteristics of large droplets with digital inline holographic imaging. Cold Reg Sci Technol 191:103373

Quetzeri-Santiago MA, Castrejón-Pita AA, Castrejón-Pita JR (2019) The effect of surface roughness on the contact line and splashing dynamics of impacting droplets. Sci Rep 9(1):1–10

Chen N, Chen H, Amirfazli A (2017) Drop impact onto a thin film: miscibility effect. Phys Fluids 29(9):092106

Mundo C, Sommerfeld M, Tropea C (1995) Droplet-wall collisions: experimental studies of the deformation and breakup process. Int J Multiph Flow 21(2):151–173